Individual Channel Design-Based Precise Analysis and Design for Three-Phase Grid-Tied Inverter With *LCL*-Filter Under Unbalanced Grid Impedance

Weimin Wu, *Member, IEEE*, Jiahao Liu, Yun Li, and Frede Blaabjerg, *Fellow, IEEE*

***Abstract*—Three-phase grid-tied inverter with *LCL* filter is usually designed to operate under symmetric grid impedance. However, in actual operations, the equivalent three-phase grid impedance tends to be unbalanced, which turns the three-phase grid-tied inverter with *LCL* filter into a highly coupled multiple-input-multiple-out system. Traditionally, the impact of the cross-coupling on the stability is directly overlooked, which may lead to imprecise stability analysis. To overcome this issue, this article proposes an analysis and design method for three-phase grid-tied inverter with *LCL* filter under the unbalanced grid impedance based on the individual channel analysis and design. First, the effect of unbalanced grid impedance on the structural robustness is comprehensively evaluated. Then, the control system is simplified with no loss of structural information. Thus, the stability can be precisely analyzed and, simultaneously, the controller parameters can be easily tuned by applying Bode/Nyquist plots. Simulation and experimental results are provided to demonstrate the validity and effectiveness of the proposed method.**

***Index Terms*—Individual channel analysis and design (ICAD), *LCL* filter, stability analysis, unbalanced grid impedance.**

I. Introduction

With the dramatic development of the distributed power generation systems, the grid-tied inverters have been increasingly employed as efficient and flexible grid interfaces in the power system [1]. In order to attenuate the switching frequency harmonics, a passive power filter is usually inserted between the inverter and the grid [2]. Compared with an *L* filter, an *LCL* filter is extensively adopted in grid-tied inverters since it can provide better harmonic attenuation with reduced inductance [3]–[5]. However, the resonance hazard of the *LCL* filter may result in stability issues. Aiming to address this challenge, a large number of innovative damping techniques have been proposed [6]–[12].

Besides the stable operation aforementioned, an additional difficulty is that, in an actual distributed power grid, the grid impedance might vary in a wide range [13], which results in a wide range variation of the resonance frequency and may challenge the stability and control performances [10]. Under these situations where the grid impedance varies widely, the uncertainty of the equivalent grid impedance is an important concern to be addressed. To keep high performance and obtain strong robustness against grid impedance variation, Pan *et al*. [14] proposed an optimized controller design for grid-tied inverters, and a specific gain for capacitor-current-feedback active damping is selected to achieve the goal. Liu *et al*. [15] put forward a single-loop current control with a hybrid damper for a single-phase grid-tied inverter, particularly when there are higher order background harmonic voltages at the point of common coupling (PCC) and when the equivalent grid impedance widely varies. In the applications of three-phase grid-tied inverters, Saïd-Romdhane *et al*. [16] proposed a systematic design procedure for the capacitor current feedback active damping of voltage-oriented PI control to ensure stable operation under severe grid inductance variations. In [17], Sadabadi *et al*. presented a robust control strategy to overcome the stability issues and decouple the *d* and *q* channels of the control system, which can guarantee stability and satisfactory transient performance against the variations of grid impedance. In [18], Adib *et al*. developed a reduced-order model for grid-tied inverters using the balanced truncation technique, while preserving the overall system stability in the case of grid impedance variations.

All aforementioned methods are proposed based on the model of single-phase grid-tied inverter or three-phase grid-tied inverter with balanced grid impedance. In these cases, the model can be simplified as single-input single-output (SISO) system, thus the classical concepts, such as the open-loop stability, gain, and phase margins, can be utilized. However, these methods may be inapplicable for the three-phase grid-tied inverter under unbalanced grid impedance, since it possess highly cross-coupled multiple-input-multiple-output (MIMO) characteristic. This indicates that the traditional methods, in which the system is assumed symmetrical or the cross-coupling is neglected when analyzing the stability and designing the controller, may result in imprecise stability analysis under unbalanced grid impedance.

Manuscript received April 28, 2019; revised July 28, 2019; accepted September 11, 2019. Date of publication September 19, 2019; date of current version February 11, 2020. This work was supported in part by the National Natural Science Foundation of China under Grants 51877130 and 51561165013, in part by Shanghai Science and Technology Commission under Grant 17040501500, and in part by the National Key Research and Development Project of China under Grant 2017YFGH001164. Recommended for publication by Associate Editor Y. Tang. *(Corresponding author: Weimin Wu.)*

W. Wu and J. Liu are with the Electrical Engineering Department, Shanghai Maritime University, Shanghai 201306, China (e-mail: wmwu@shmtu.edu.cn; dqgc2013ljh@126.com).

Y. Li is with the HiTrend Technology (Shanghai) Co., Ltd., Shanghai 201203, China (e-mail: yun09111025@163.com).

F. Blaabjerg is with the Energy Engineering Department, Aalborg University, Aalborg 9100, Denmark (e-mail: fbl@et.aau.dk).

Color versions of one or more of the figures in this article are available online at http://ieeexplore.ieee.org.

Digital Object Identifier 10.1109/TPEL.2019.2942602

In fact, in a three-phase distributed power generation system, due to the unbalanced power line impedance, three-phase asymmetrical loads, single-phase loads, single-phase grid-tied inverters, and multiple paralleled inverters connected to PCC, the equivalent three-phase grid impedance tends to be unbalanced. A previous research based on the impedance analysis has proved that the unbalanced grid impedance will reduce the stability of the three-phase grid-tied inverter system [19]. Therefore, it is vital to develop effective analysis and design method for the three-phase grid-tied inverter under unbalanced grid impedance.

According to [19], the stability analysis of three-phase grid-tied inverter with *L* filter under unbalanced grid impedance can be addressed by harmonic linearization technique. However, the model derivation is complicated, especially when it is extended to *LCL*-filtered grid-tied inverter. Liu *et al*. [20] proposed a modeling method for a three-phase grid-tied inverter with *L* filter under unbalanced grid impedance, then the stability can be analyzed based on the eigenvalues of open-loop transfer function matrix by utilizing the Generalized Nyquist Criterion (GNC). Nevertheless, it is not easy to apply the proposed modeling method to *LCL*-filter-based grid-tied inverter. In [21], Jin *et al*. proved that the unbalanced loads would bring adverse effect on the stability of the system when the grid impedance was not negligible, and the active imbalance compensation was adopted to improve the stability. Nevertheless, the paper has not investigated the impact of the grid impedance variation on the robustness and stability.

Motivated by the aforementioned limitations, this article proposes an analysis and design method for a three-phase grid-tied inverter with *LCL* filter under the unbalanced grid impedance based on the individual channel analysis and design (ICAD). The effect of the cross-coupling, introduced by unbalanced grid impedance, is explicitly addressed. First, the impact of unbalanced grid impedance on the structural robustness is comprehensively evaluated. To significantly enhance the robustness, the optimal passive damping is used. Then, by utilizing the ICAD approach, the highly cross-coupled MIMO system is decomposed into two SISO subsystems, which significantly simplifies the control system. Meanwhile, the multivariable nature of the original plant is maintained in the equivalent subsystems with no loss of structural information. Thus, the stability can be precisely analyzed and, simultaneously, the controller parameters can be easily tuned by applying Bode/Nyquist plots. The new findings and major contributions of this article are highlighted below.

1) The proposed method enables to design two separated SISO subsystems instead of applying multivariable control theory for analysis and design of MIMO systems. The stability analysis and controller parameters tuning for *LCL*-filtered grid-tied inverter under unbalanced grid impedance are remarkably simplified.
2) This article reveals that when analyzing the stability and tuning the controller parameters, directly neglecting the cross-coupling leads to imprecise results. Compared with the traditional method that ignores the coupling, the proposed method can provide more precise stability analysis under unbalanced grid impedance by independently analyzing the individual channels.

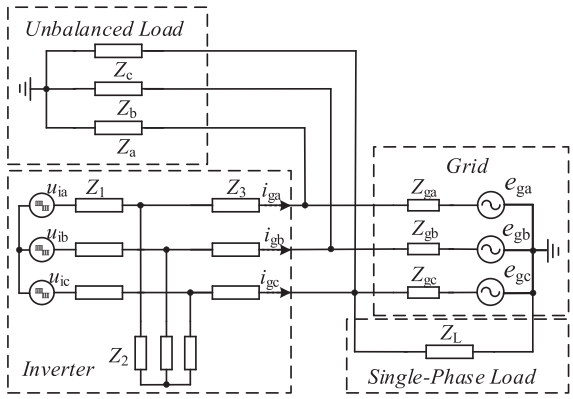

Fig. 1. Topology of the three-phase grid-tied inverter with unbalanced loads connected to PCC.

3) It is found that by independently tuning the current controller parameters, the gain and phase margins as well as the bandwidths of α- and β-axes are almost equal under unbalanced grid impedance, thus the better control performance can be achieved.
4) The theoretical analysis reveals that the unbalanced grid impedance deteriorates the structural robustness of the *LCL*-filtered grid-tied inverter, especially under the severely unbalanced case. Simultaneously, this article proves that robustness can be improved by utilizing passive damping.

The rest of this article is organized as follows. Section II summarizes the main reasons which significantly lead to the unbalanced grid impedance. In Section III, the issues caused by *LCL* filter-based grid-tied inverter under unbalanced grid impedance are presented. Then, the precise analysis and design method based on ICAD is proposed in Section IV. In Section V, the different design methods are compared to highlight the significant advantage of the proposed method. The effectiveness and accuracy of the proposed method are demonstrated by a series of simulation and experimental results in Section VI. Section VII gives a detailed discussion on some new findings. Finally, the conclusions are drawn in Section VIII.

II. Main Reasons of the Unbalanced Grid Impedance

A lot of previous researches are based on a fundamental assumption that the three-phase grid impedance is balanced. However, this may be impossible to be always satisfied in the actual distributed power generation systems, since the parameter variation, unbalanced loads, and power line impedance are inevitable. This section summarizes the main reasons that significantly cause the imbalance of equivalent grid impedance.

A. Unbalanced Loads [21] and Power Line Impedance

Fig. 1 illustrates the topology of the three-phase grid-tied inverter with unbalanced loads connected to PCC. Z_a, Z_b, Z_c, and Z_L represent the three-phase unbalanced load and single-phase load, respectively. u_i and e_g are inverter output voltage and grid voltage. Z_1, Z_2, and Z_3 are the impedances of inverter-side

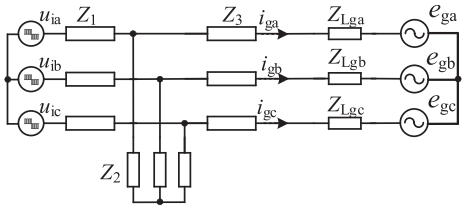

Fig. 2. Topology of equivalent standard model with unbalanced grid impedance.

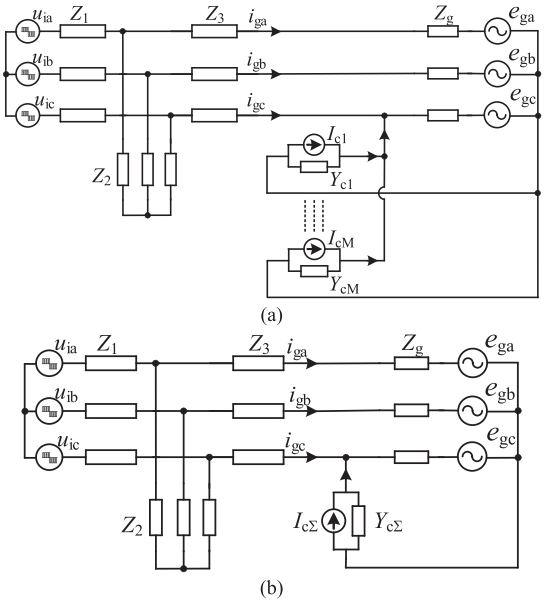

Fig. 3. Topology of three-phase distributed power grid with *M*-paralleled single-phase grid-tied inverters connected to Phase C. (a) Original model. (b) Equivalent model.

inductor, filter capacitor, and grid-side inductor, respectively. i_{ga}, i_{gb}, and i_{gc} are grid-injected currents. Z_{ga}, Z_{gb}, and Z_{gc} denote the unbalanced power line impedance of per-phase. It is obvious that the equivalent grid impedance is unbalanced, and one can easily derive the equivalent standard model as shown in Fig. 2, where Z_{Lga}, Z_{Lgb}, and Z_{Lgc} represent the unbalanced equivalent grid impedance.

B. Unbalanced Equivalent Grid Impedance Caused by Single-Phase Grid-Tied Inverters Connected to PCC

A three-phase distributed power grid system may contain a number of single-phase grid-tied inverters. Fig. 3 presents the topology of three-phase distributed power grid with *M*-paralleled single-phase grid-tied inverters connected to Phase C. In which, the *M*-paralleled single-phase grid-tied inverters are described with the Norton equivalent model. In Fig. 3, I_{ci} (i = 1 …*M*) and $I_{c\Sigma}$ denote the currents of each single-phase grid-tied inverter and the sum of I_{ci}, respectively; Y_{ci} (i = 1 …*M*) and $Y_{c\Sigma}$ denote the output admittances of each single-phase grid-tied inverter and the sum of Y_{ci}, respectively. In order to conveniently reveal the relationship between the equivalent grid impedance and M-paralleled single-phase grid-tied inverters, the equivalent model in Fig. 3(b) is transformed into the standard model with

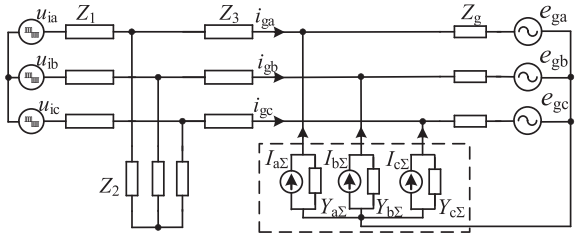

Fig. 4. Equivalent model of three-phase distributed power grid with *M*1-, *M*2-, and *M*3-paralleled single-phase grid-tied inverters connected to Phases A, B, and C, respectively.

unbalanced grid impedance in Fig. 2, where

$$\begin{cases} Z_{Lga} = Z_g \\ Z_{Lgb} = Z_g \\ Z_{Lgc} = \dfrac{3Z_2u_{ic}+[3Z+(Z_1+Z_2)Z_g]\cdot(I_{c\Sigma}-e_{gc}Y_{c\Sigma})+T}{3Z_2u_{ic}(1+Y_{c\Sigma}Z_g)-Z_g(Z_1+Z_2)(2I_{c\Sigma}-e_{ga}Y_{c\Sigma}-e_{gb}Y_{c\Sigma})+T} \\ \qquad \cdot Z_g \end{cases} \tag{1}$$

where $Z = Z_1Z_2 + Z_1Z_3 + Z_2Z_3$ and $T = (e_{g\Sigma} - 3e_{gc})(Z_1 + Z_2)$.

It can be obtained from (1) that the *M*-paralleled single-phase grid-tied inverters connected to Phase C will significantly change its grid impedance, while the equivalent grid impedances of Phases A and B remain unchanged, which forces the balanced grid impedance into unbalanced one. This fact indicates that the single-phase grid-tied inverters connected to PCC can result in the equivalent unbalanced grid impedance. Additionally, in practice, the number *M* of the single-phase grid-tied inverters connected to Phase C may vary, which results in $I_{c\Sigma}$ and $Y_{c\Sigma}$ varying, too. Consequently, according to (1), Z_{Lgc} varies widely, as well.

Further, the more complicated case is considered. In Fig. 4, M1-, M2-, and M3-paralleled single-phase grid-tied inverters are connected to Phases A, B, and C, respectively. $I_{a\Sigma}$, $I_{b\Sigma}$, and $I_{c\Sigma}$ denote the currents generated by the single-phase grid-tied inverters connected to Phases A, B, and C, respectively; $Y_{a\Sigma}$, $Y_{b\Sigma}$, and $Y_{c\Sigma}$ represent the output admittances of single-phase grid-tied inverters connected to per-phase. Then, the equivalent grid impedance can be deduced as

$$\begin{cases} Z_{Lga} \\ \quad = \dfrac{[3Z_2u_{ia}+3Z(I_{a\Sigma}-e_{ga}Y_{a\Sigma})+Z_g(Z_1+Z_2)\cdot(I_\Sigma-e_gY_\Sigma)+T_a]\cdot Z_g}{3Z_2u_{ia}(1+Y_{a\Sigma}Z_g)-Z_g(Z_1+Z_2)(3I_{a\Sigma}-I_\Sigma-e_{gb}Y_{a\Sigma}-e_{gc}Y_{a\Sigma})+T_a} \\ Z_{Lgb} \\ \quad = \dfrac{[3Z_2u_{ib}+3Z(I_{b\Sigma}-e_{gb}Y_{b\Sigma})+Z_g(Z_1+Z_2)\cdot(I_\Sigma-e_gY_\Sigma)+T_b]\cdot Z_g}{3Z_2u_{ib}(1+Y_{b\Sigma}Z_g)-Z_g(Z_1+Z_2)(3I_{b\Sigma}-I_\Sigma-e_{ga}Y_{b\Sigma}-e_{gc}Y_{b\Sigma})+T_b} \\ Z_{Lgc} \\ \quad = \dfrac{[3Z_2u_{ic}+3Z(I_{c\Sigma}-e_{gc}Y_{c\Sigma})+Z_g(Z_1+Z_2)\cdot(I_\Sigma-e_gY_\Sigma)+T_c]\cdot Z_g}{3Z_2u_{ic}(1+Y_{c\Sigma}Z_g)-Z_g(Z_1+Z_2)(3I_{c\Sigma}-I_\Sigma-e_{ga}Y_{c\Sigma}-e_{gb}Y_{c\Sigma})+T_c} \end{cases} \tag{2}$$

where $I_\Sigma = I_{a\Sigma} + I_{b\Sigma} + I_{c\Sigma}$, $e_gY_\Sigma = e_{ga}Y_{a\Sigma} + e_{gb}Y_{b\Sigma} + e_{gc}Y_{c\Sigma}$, $u_{ia} + u_{ib} + u_{ic} = 0$, $T_i = (e_{g\Sigma} - 3e_{gi})(Z_1 + Z_2)$ $i = a, b, c$, and $e_{g\Sigma} = e_{ga} + e_{gb} + e_{gc}$.

In practical applications, the numbers M1, M2, and M3 of the single-phase grid-tied inverters connected to Phases A, B, and C are generally different, thus the currents $I_{a\Sigma}$, $I_{b\Sigma}$, and $I_{c\Sigma}$ and output admittances $Y_{a\Sigma}$, $Y_{b\Sigma}$, and $Y_{c\Sigma}$ are different

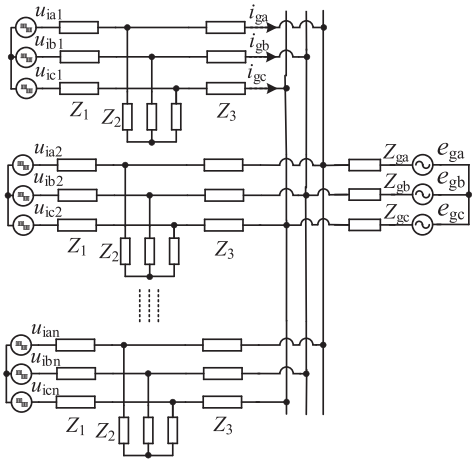

Fig. 5. Topology of *N*-paralleled grid-tied inverters.

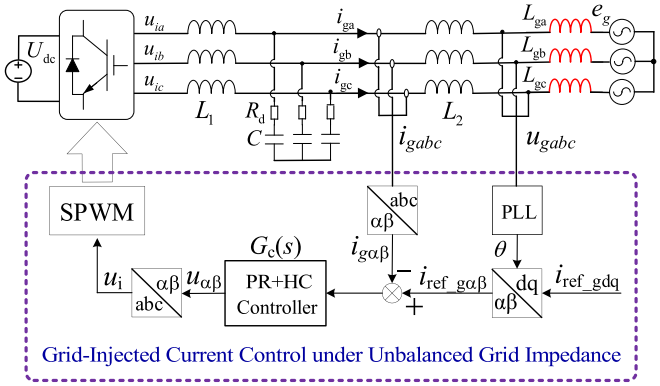

Fig. 6. Topology and control scheme of three-phase *LCL*-type grid-tied inverter under unbalanced grid impedance.

as well. According to (2), the equivalent grid impedance is unbalanced. Similarly, the number M1, M2, and M3 may vary in practical applications, which leads to Z_{Lga}, Z_{Lgb}, and Z_{Lgc} wide variation, as well. Thus, the controller of three-phase grid-tied inverter applied in this case needs to be elaborately designed to adapt the varying and unbalanced grid impedance.

C. Unbalanced Equivalent Grid Impedance Amplified by the N-Paralleled Grid-Tied Inverters

Next, a set of *N*-paralleled grid-tied inverters with an *LCL* filter is discussed. The dynamic of these inverters is coupled due to the unbalanced grid impedance. Fig. 5 presents the topology of *N*-paralleled grid-tied inverters. It is reasonable to assume that all the installed inverters are identical, not only their impedances but also their hardware and software. In this scenario, the output voltages of all inverters may be considered equal, i.e., $u_{iaj} = u_{ia1}$, $u_{ibj} = u_{ib1}$, and $u_{icj} = u_{ic1}$ (j = 2 …*N*). And then, according to the superposition principle and Thévenin equivalent circuits [22], one can transfer the circuit in Fig. 5 into the equivalent circuit in Fig. 2, in which

$$\begin{cases} Z_{Lga} = N \cdot Z_{ga} \\ Z_{Lgb} = N \cdot Z_{gb} \\ Z_{Lgc} = N \cdot Z_{gc}. \end{cases} \tag{3}$$

It is found that an equivalent single inverter whose equivalent grid impedance is *N* times bigger represents the *N* inverters. Thus, the unbalanced power line impedance will be significantly amplified by the *N*-paralleled grid-tied inverters.

III. Issues Caused by *LCL* Filter-Based Grid-Tied Inverter Under Unbalanced Grid Impedance

A. System Description

Fig. 6 depicts a three-phase voltage-source inverter connected into the grid under unbalanced grid impedance through an *LCL* filter. L_1 is the inverter-side inductor, C is the filter capacitor, L_2 is the grid-side inductor, and R_d is the damping resistor.

TABLE I
Parameters of the System

Symbol	Description	Value
e_g	Grid voltage	220 V(RMS)
U_{dc}	DC-link voltage	700 V
L_1	Inverter-side inductor	2.4 mH
L_2	Grid-side inductor	2.4 mH
C	Filter capacitor	2 μF
R_d	Damping resistor	5 Ω
L_{ga}	Impedance of Phase A	4 mH
L_{gb}	Impedance of Phase B	4 mH
L_{gc}	Impedance of Phase C	[4 mH, 8 mH]
f_0	Grid frequency	50 Hz
f_{sw}	Switching frequency	10 kHz
f_s	Sampling frequency	10 kHz

i_{ga}, i_{gb}, and i_{gc} are the grid-injected currents, U_{dc}, u_{iabc}, and u_{gabc} are dc-link, inverter output, and PCC voltages. The grid voltage e_g behaves as a disturbance, which is considered to be zero when describing the modeling and control. L_{ga}, L_{gb}, and L_{gc} denote the per-phase equivalent grid impedance, respectively. Assuming that there is a 120-kW system, and 20 sets of 220 V/50 Hz/6 kW paralleled inverters are connected to a 120-kVA grid power transformer through 200-m power line. Thus, the short-circuit impedance Z_{sc} and the cable impedance the Z_l can be determined by the following.

1) For a 120-kVA grid power transformer, the short-circuit impedance Z_{sc} is 0.15 mH (4%).
2) The cable impedance is 0.25 μH/m [15]. The 200-m power line indicates that Z_l is 0.05 mH.

Therefore, the grid impedance is calculated as 0.2 mH. Due to the parameter shift and unbalanced line impedance, we assume that the grid impedance of Phase C varies in (0.2 and 0.4 mH). According to (3), the unbalanced equivalent grid impedance can be determined. Table I presents the parameters of the system

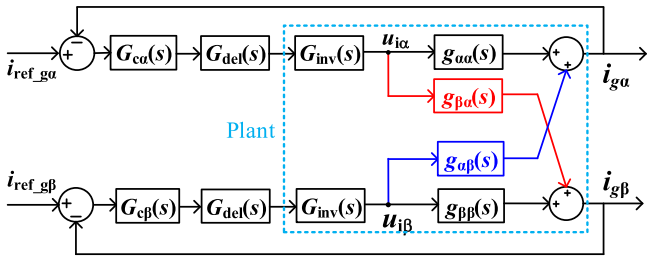

Fig. 7. Block diagram of the three-phase grid-tied inverter under unbalanced grid impedance.

under study. Apparently, greater the value of L_{gc}, the more severe is an imbalance of the grid impedance.

Note that the three-phase grid-tied inverter is an MIMO system. The relationship between the grid-injected currents and inverter output voltages can be written as

$$I_g(s) = G(s) \cdot U_i(s) \Leftrightarrow \begin{pmatrix} i_{ga} \\ i_{gb} \\ i_{gc} \end{pmatrix} = \begin{pmatrix} Y_{11}Y_{12}Y_{13} \\ Y_{21}Y_{22}Y_{23} \\ Y_{31}Y_{32}Y_{33} \end{pmatrix} \cdot \begin{pmatrix} u_{ia} \\ u_{ib} \\ u_{ic} \end{pmatrix} \tag{4}$$

where $I_g(s) = [i_{ga}, i_{gb}, i_{gc}]^T$ and $U_i(s) = [u_{ia}, u_{ib}, u_{ic}]^T$. $G(s)$ is a 3×3 admittance matrix, depicting the influence of per-phase voltage on per-phase current. According to the superposition principle, Y_{ij} $(i, j = 1, 2, 3)$ can be derived, and nondiagonal elements $Y_{12} = Y_{21}$, $Y_{13} = Y_{31}$, $Y_{23} = Y_{32}$. The detailed expressions of Y_{ij} are given in (A1.3).

The control scheme presented in Fig. 6 is developed and analyzed in the stationary reference $(\alpha\beta\gamma)$ frame. Correspondingly, substituting Clarke transformation matrix into (4), the grid-injected currents and inverter output voltages are transformed to $\alpha\beta\gamma$ frame as follows:

$$I_{g\alpha\beta\gamma}(s) = G_{\alpha\beta\gamma}(s) \cdot U_{i\alpha\beta\gamma}(s) \Leftrightarrow \begin{pmatrix} i_{g\alpha} \\ i_{g\beta} \\ i_{g\gamma} \end{pmatrix} = \begin{pmatrix} g_{\alpha\alpha}(s) & g_{\alpha\beta}(s) & 0 \\ g_{\beta\alpha}(s) & g_{\beta\beta}(s) & 0 \\ 0 & 0 & 0 \end{pmatrix} \begin{pmatrix} u_{i\alpha} \\ u_{i\beta} \\ u_{i\gamma} \end{pmatrix} \tag{5}$$

where $g_{\alpha\alpha}(s)$, $g_{\beta\beta}(s)$, $g_{\alpha\beta}(s)$, and $g_{\beta\alpha}(s)$ are presented in (A1.4).

Obviously, since the γ components of the transfer matrix $G_{\alpha\beta\gamma}(s)$ are equal to zero, which can be omitted, the admittance matrix $G(s)$ in (4) is transformed from a 3×3 transfer matrix to a 2×2 transfer matrix $G_{\alpha\beta}(s)$, i.e.,

$$I_{g\alpha\beta}(s) = G_{\alpha\beta}(s) \cdot U_{i\alpha\beta}(s) \Leftrightarrow \begin{pmatrix} i_{g\alpha} \\ i_{g\beta} \end{pmatrix} = \begin{pmatrix} g_{\alpha\alpha}(s) & g_{\alpha\beta}(s) \\ g_{\beta\alpha}(s) & g_{\beta\beta}(s) \end{pmatrix} \begin{pmatrix} u_{i\alpha} \\ u_{i\beta} \end{pmatrix}. \tag{6}$$

Hence, the three-phase grid-tied inverter system under unbalanced grid impedance can be seen as a standard 2-intput 2-output multivariable system, whose closed-loop block diagram with a diagonal controller $G_c(s)$ is shown in Fig. 7. $G_{\text{inv}}(s)$ is the transfer function of the PWM inverter [23]. In this article, the three-phase sine-triangle pulsewidth modulation is adopted, thus $G_{\text{inv}}(s)$ can be expressed as

$$G_{\text{inv}}(s) = \frac{U_{\text{dc}}}{2V_{\text{tri}}} \tag{7}$$

where V_{tri} is the amplitude of the triangle carrier.

$G_{\text{del}}(s)$ is the digital time delay, including the computational delay and modulation delay [9], and it is commonly expressed as

$$G_{\text{del}}(s) = e^{-\lambda T_s s} \tag{8}$$

where T_s is the sampling period, and λ is the delay time normalized with T_s. The normal value of λ is selected as 1 or 1.5 in a real operation [24].

In this article, the proportional resonant regulator with a harmonic compensator (PR+HC regulator) is adopted as the current controller. Thus, the diagonal controller $G_c(s)$ is defined as

$$G_c(s) = \begin{bmatrix} G_{c\alpha}(s) & \\ & G_{c\beta}(s) \end{bmatrix} = \begin{bmatrix} K_{p\alpha} + \sum\limits_{h=1,3,5,7,9} \dfrac{K_{i\alpha h} s}{s^2 + (\omega_0 h)^2} & \\ & K_{p\beta} + \sum\limits_{h=1,3,5,7,9} \dfrac{K_{i\beta h} s}{s^2 + (\omega_0 h)^2} \end{bmatrix} \tag{9}$$

where ω_0 is the grid angular frequency; $K_{p\alpha}$ and $K_{p\beta}$ are the proportional gains; $K_{i\alpha h}$ and $K_{i\beta h}$ are the resonant gains for the h-order harmonic.

It should be pointed out that the effect of PLL and coupling between the PCC voltage u_{gabc} and grid-injected current i_{gabc} have been neglected in this article. According to [25], the dynamics of the PLL and the coupling effect between u_{gabc} and i_{gabc} significantly decrease as the grid stiffness (which is characterized by the short-circuit ratio, SCR) increases. Under the stiff grid condition (SCR > 3), when analyzing the stability and tuning the control parameters, the impact of PLL and coupling between u_{gabc} and i_{gabc} due to grid impedance can be ignored [26], [27]. In this article, under the study with $L_{ga} = L_{gb} = 4$ mH, $L_{gc} = 8$ mH, the SCR is equal to 13, which indicates that the grid can be considered as a stiff grid. Thus, based on the stiff grid condition, it is reasonable and acceptable to neglect the effect of PLL and coupling between u_{gabc} and i_{gabc}.

B. Significant Issues Raised by Unbalanced Grid Impedance

Fig. 8 shows the Bode plots of the $g_{\alpha\alpha}(s)$, $g_{\beta\beta}(s)$, $g_{\alpha\beta}(s)$, and $g_{\beta\alpha}(s)$ defined in (5) with $R_d = 0$ and unbalanced grid impedance. It can be observed that there exist two resonant frequencies, which are expressed as

$$\omega_{\text{res1}} = \sqrt{\frac{A \cdot L_1 + B + \sqrt{A^2 - 3B}}{B \cdot L_1 \cdot C}}$$
$$\omega_{\text{res2}} = \sqrt{\frac{A \cdot L_1 + B - \sqrt{A^2 - 3B}}{B \cdot L_1 \cdot C}} \tag{10}$$

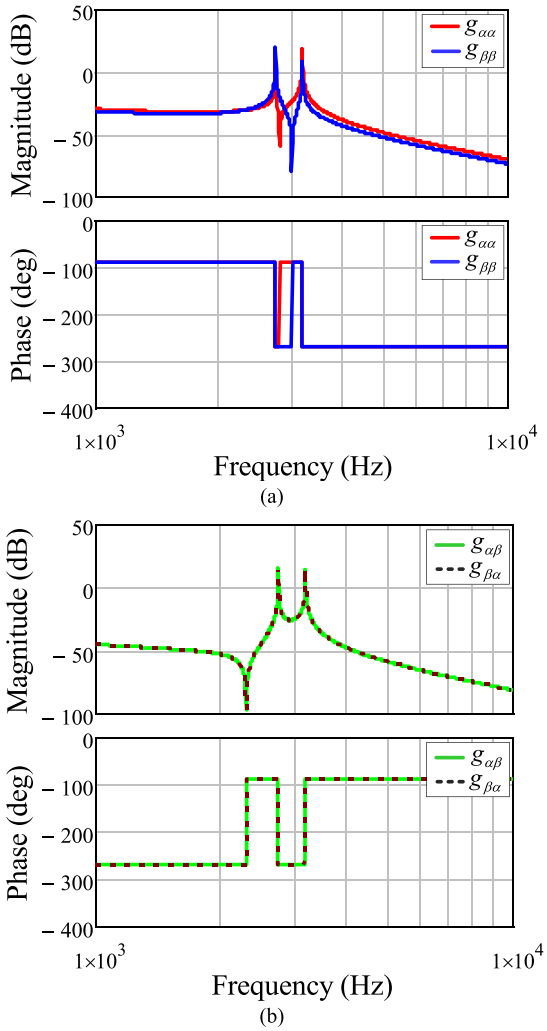

Fig. 8. Bode plots of each component of admittance matrix $G(s)$ under unbalanced grid impedance. (a) Bode plots of $g_{\alpha\alpha}(s)$ and $g_{\beta\beta}(s)$. (b) Bode plots of $g_{\alpha\beta}(s)$ and $g_{\beta\alpha}(s)$.

where $A = 3L_2 + L_{ga} + L_{gb} + L_{gc}$ and $B = (L_2 + L_{ga})(L_2 + L_{gb}) + (L_2 + L_{ga})(L_2 + L_{gc}) + (L_2 + L_{gb})(L_2 + L_{gc})$.

Distinctly, the multiple resonant behaviors make it much more complicated to precisely design high-performance current controller. In addition, the resonances appear in the coupling terms at the same time, thus the stability may deteriorate with the loop interaction under the unbalanced grid impedance condition. These indicate that the stability of the system will be subject to multiple resonant behaviors and loop cross-coupling. Then, following series of issues arise:

1) precise design of the current controller;
2) stability evaluation of this highly coupled system;
3) quantification of the interaction effect superimposed on each controlled loop.

Traditionally, the system is assumed symmetrical or the coupling terms $g_{\alpha\beta}(s)$ and $g_{\beta\alpha}(s)$ are neglected when analyzing the stability and designing the controller. Therefore, the three-phase grid-tied inverter can be directly simplified as two SISO subsystems and the Bode diagram or root locus method can

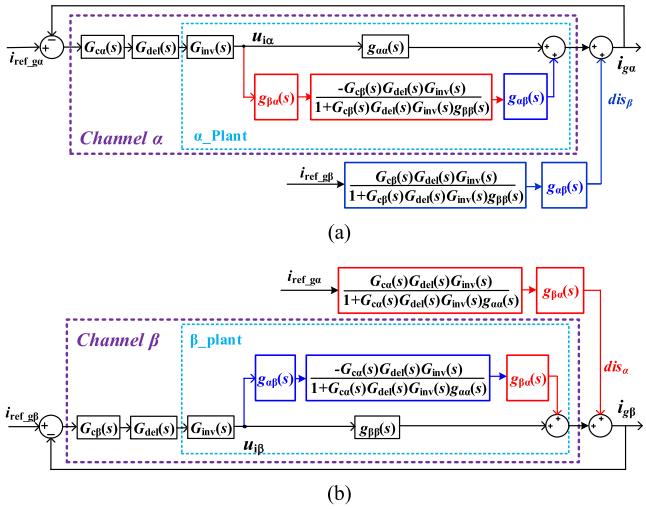

Fig. 9. Equivalent individual channel representation. (a) Channel α in α-axis. (b) Channel β in β-axis.

be easily applied to analyze the stability and tune the controller [28], [29]. However, this may be infeasible under the unbalanced grid impedance since the simplification will directly ignore the impact of the cross-coupling terms on the grid-injected current dynamics, which may bring about imprecise assessment. It is, therefore, vital to develop a simple and effective analysis method on the stability, robustness, and cross-coupling under the unbalanced grid impedance condition.

IV. Proposed Precise Analysis and Design Method Based on ICAD

To address the aforementioned issues, this article proposes a precise analysis and design method based on ICAD for three-phase grid-tied inverter under the unbalanced grid impedance. The ICAD is a frequency domain-oriented framework [30], [31], which can be utilized to investigate the potential and limitations for feedback design of MIMO system, formulate a preferable analytical structure, and provide a solution methodology for the stability evaluation [32]–[34]. More details could be found in [30]–[35], which fall beyond the scope of this article.

A. Analysis Based on ICAD

According to the block diagram in Fig. 7, the forward signal transmission from $i_{\mathrm{ref\_}g\alpha}(s)$ to $i_{g\alpha}(s)$ follows two parallel paths: one directly via $g_{\alpha\alpha}(s)$; the other through $g_{\beta\alpha}(s)$, the bottom feedback subsystem, and $g_{\alpha\beta}(s)$. In addition, it can be found that the forward cross-signal transmission from $i_{\mathrm{ref\_}g\beta}(s)$ to $i_{g\alpha}(s)$ is through the bottom feedback subsystem and $g_{\alpha\beta}(s)$. These signal transmissions from $i_{\mathrm{ref\_}g\alpha}(s)$ to $i_{g\alpha}(s)$ and $i_{\mathrm{ref\_}g\beta}(s)$ to $i_{g\alpha}(s)$ are restructured as depicted in Fig. 9(a), which denoted the individual channel α, together with the additive signal $\mathrm{dis}_\beta(s)$. Likewise, the individual channel β from $i_{\mathrm{ref\_}g\beta}(s)$ to $i_{g\beta}(s)$, together with the additive signal $\mathrm{dis}_\alpha(s)$, is represented in Fig. 9(b).

Hence, the 2 × 2 MIMO system is then decomposed into two SISO subsystems. It enables to design two separated SISO subsystems instead of applying multivariable control theory for analysis and design of MIMO systems. The generalized plant of each SISO subsystem is expressed as

$$\begin{aligned} G_{\alpha\text{plant}}(s) &= G_{\text{inv}}(s) \\ &\times \left(g_{\alpha\alpha}(s) - \frac{g_{\beta\alpha}(s)g_{\alpha\beta}(s)G_{c\beta}(s)G_{\text{del}}(s)G_{\text{inv}}(s)}{1 + G_{c\beta}(s)G_{\text{del}}(s)G_{\text{inv}}(s)g_{\beta\beta}(s)} \right) \\ G_{\beta\text{plant}}(s) &= G_{\text{inv}}(s) \\ &\times \left(g_{\beta\beta}(s) - \frac{g_{\alpha\beta}(s)g_{\beta\alpha}(s)G_{c\alpha}(s)G_{\text{del}}(s)G_{\text{inv}}(s)}{1 + G_{c\alpha}(s)G_{\text{del}}(s)G_{\text{inv}}(s)g_{\alpha\alpha}(s)} \right). \end{aligned} \tag{11}$$

It is worth noting that there is no assumption or loss of multivariable information when deriving the equivalent individual channel representation, which is a significant advantage over the traditional design methods, where the loop interactions are assumed very small and negligible.

Furthermore, the open-loop transfer functions of channels α and β can be represented as

$$\begin{aligned} T_\alpha(s) &= G_{c\alpha}(s)G_{\text{del}}(s)G_{\alpha\text{plant}}(s) \\ &= G_{c\alpha}(s)G_{\text{del}}(s)G_{\text{inv}}(s)g_{\alpha\alpha}(s)(1 - \gamma(s)h_\beta(s)) \end{aligned} \tag{12}$$

$$\begin{aligned} T_\beta(s) &= G_{c\alpha}(s)G_{\text{del}}(s)G_{\beta\text{plant}}(s) \\ &= G_{c\beta}(s)G_{\text{del}}(s)G_{\text{inv}}(s)g_{\beta\beta}(s)(1 - \gamma(s)h_\alpha(s)) \end{aligned} \tag{13}$$

where

$$\gamma(s) = \frac{g_{\alpha\beta}(s)g_{\beta\alpha}(s)}{g_{\alpha\alpha}(s)g_{\beta\beta}(s)}s \tag{14}$$

$$h_\alpha(s) = \frac{G_{c\alpha}(s)G_{\text{del}}(s)G_{\text{inv}}(s)g_{\alpha\alpha}(s)}{1 + G_{c\alpha}(s)G_{\text{del}}(s)G_{\text{inv}}(s)g_{\alpha\alpha}(s)} \tag{15}$$

$$h_\beta(s) = \frac{G_{c\beta}(s)G_{\text{del}}(s)G_{\text{inv}}(s)g_{\beta\beta}(s)}{1 + G_{c\beta}(s)G_{\text{del}}(s)G_{\text{inv}}(s)g_{\beta\beta}(s)}. \tag{16}$$

In (14), $\gamma(s)$ is called the multivariable structure function (MSF) [32], whose magnitude quantifies the cross-coupling between channels α and β. $\gamma(s)$ inherently reveals important natures on the structural robustness. The structural robustness can be guaranteed if $\gamma(s)$ complies the following constrain conditions:

1) $\gamma(s)$ has no right-hand plane poles;
2) the Nyquist plot of $\gamma(s)$ does not encircle nor pass near the point (1, 0).

If the Nyquist plot of $\gamma(s)$ crosses near point (1, 0), the structural robustness is poor [33]. Thus, to achieve strong robustness, the γ(s) is required not to encircle nor pass near (1, 0).

B. Enhance the Structural Robustness by Utilizing the Passive Damper R_d

As discussed in the above list, the (1) and (2) can be utilized to assess the structural robustness. It is easy to prove that (1) is satisfied. Then, it is necessary to reckon the closeness of $\gamma(s)$ to (1, 0) to evaluate the structural robustness, since the proximity of $\gamma(s)$ to (1, 0) in the Nyquist plot demonstrates to what extent the plant structure is sensitive to uncertainty. To this end, consider $\gamma(s)$ evaluated at $s = jw$ as follows:

$$\gamma(jw) = \frac{\text{Re}_n + j\text{Im}_n}{\text{Re}_d + j\text{Im}_d} \tag{17}$$

where

$$\begin{aligned} \text{Re}_d &= k_1\omega^4 - (k_2R_d^2 + k_3)\omega^2 + k_4 \\ \text{Im}_d &= -k_5R_d\omega^3 + k_6R_d\omega \\ \text{Re}_n &= k_7\omega^4 - (k_8R_d^2 + k_9)\omega^2 + k_{10} \\ \text{Im}_n &= -k_{11}R_d\omega^3 + k_{12}R_d\omega \end{aligned}$$

and $k_1 - k_{12}$ are real positive constants. Among them, k_1 and k_7 will be used next, which are given as follows:

$$\begin{aligned} k_1 &= C^2L_1^2[4L_2(3L_2 + 2L_{ga} + 2L_{gb} + 2L_{gc}) \\ &\quad + (L_{gb} + L_{gc})(4L_{ga} + L_{gb} + L_{gc})] \\ k_7 &= C^2L_1^2(L_{gb} - L_{gc})^2. \end{aligned} \tag{18}$$

Then, the argument of $\gamma(s)$ can be derived as

$$\arg[\gamma(jw)] = \tan^{-1}\left(\frac{\text{Im}_n}{\text{Re}_n}\right) - \tan^{-1}\left(\frac{\text{Im}_d}{\text{Re}_d}\right). \tag{19}$$

Thus,

$$\begin{cases} \lim_{\omega\to\infty}\left(\frac{\text{Im}_n}{\text{Re}_n}\right) = 0 \\ \lim_{\omega\to\infty}\left(\frac{\text{Im}_d}{\text{Re}_d}\right) = 0 \end{cases} \Rightarrow \lim_{\omega\to\infty}(\arg[\gamma(jw)]) = 0. \tag{20}$$

Correspondingly, the magnitude of $\gamma(s)$ yields

$$\begin{aligned} \lim_{\omega\to\infty}\|\gamma(jw)\| &= \frac{k_7}{k_1} \\ &= \frac{(L_{gb} - L_{gc})^2}{\begin{array}{r}4L_2(3L_2 + 2L_{ga} + 2L_{gb} + 2L_{gc}) \\ +(L_{gb} + L_{gc})(4L_{ga} + L_{gb} + L_{gc})\end{array}}. \end{aligned} \tag{21}$$

Here, a structural robustness measure M_{SMF} is defined as

$$M_{\text{MSF}} = \lim_{\omega\to\infty}\|\gamma(jw)\|. \tag{22}$$

It can be easily observed from (20) to (22) that the Nyquist trajectory of $\gamma(s)$ crosses the point (M_{MSF}, 0). Thus, considering that the grid impedance of Phase C varies within a wide range as listed in Table I, when assessing the structural robustness, it is necessary to investigate the relationship between M_{MSF} and L_{gc}.

Obviously, according to (21), M_{SMF} increases as the value of L_{gc} does. And M_{MSF} has an upper limit, i.e.,

$$\lim_{L_{gc}\to\infty} M_{\text{MSF}} = 1. \tag{23}$$

Hence, when L_{gc} tends to infinity, the Nyquist trajectory of $\gamma(s)$ will cross the point (1, 0). However, this will never happen in an actual distributed power grid, which reveals that the trajectory will not encircle (1, 0).

Based on the aforementioned analysis, a conclusion can be drawn that greater the value of L_{gc}, the closer the trajectory

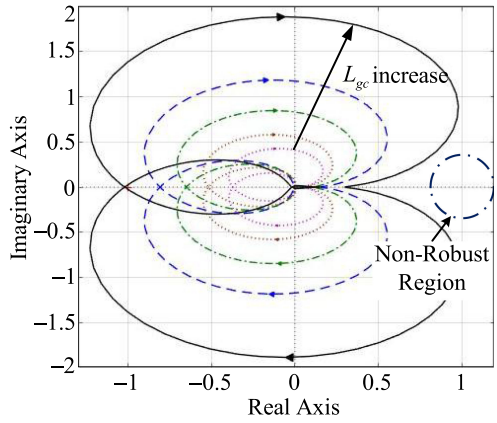

Fig. 10. Nyquist plots of $\gamma(s)$ with different values of L_{gc} and a fixed R_d.

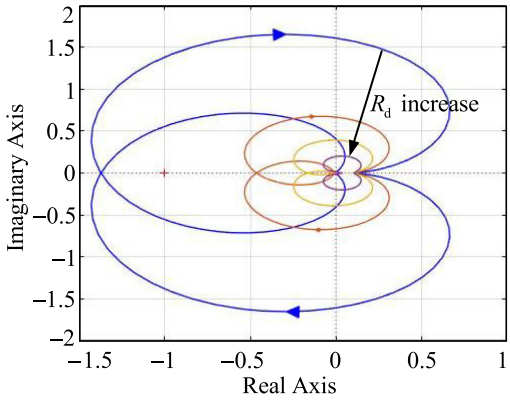

Fig. 11. Nyquist plots of $\gamma(s)$ with different values of R_d and a fixed L_{gc}.

is to (1, 0) and the poorer structural robustness is. In order to intuitively illustrate the observations, the Nyquist plots of $\gamma(s)$ with different values of L_{gc} and a fixed R_d are presented in Fig. 10.

It has been shown that the closeness to (1, 0) and gain margin of $\gamma(s)$ decrease as the value of L_{gc} increases. The Nyquist trajectory passes near (1, 0), even crosses the nonrobust region under the great value of L_{gc}, which is consistent with the theoretical analysis.

In order to improve the structural robustness, the passive damper R_d is adopted. Fig. 11 shows the Nyquist plots of $\gamma(s)$ with different values of R_d and a fixed L_{gc}. It can be found that greater the value of R_d, the farther the trajectory away from (1, 0) and nonrobust region is. Thus, the structural robustness enhances as the value of R_d increases. However, the increasing resistor R_d means more power losses and deterioration of high-frequency harmonic attenuation ability. Here, an optimal R_d can be determined by the equivalent Q-factor method, which is given by

$$Q_E = \frac{1}{R_E}\sqrt{\frac{L_E}{C_E}} \tag{24}$$

where Q_E is the equivalent Q-factor, R_E, L_E, and C_E are the equivalent resistor, inductance, and capacitance of an equivalent series *LCR* circuit, respectively.

TABLE II
OPEN-LOOP CHANNEL ZEROES AND POLES

Channel	Zeroes	Poles
α	Zeroes of $G_{c\alpha}(s)(1-\gamma(s)h_\beta(s))$	Poles of $g_{\alpha\alpha}(s)$, $g_{\alpha\beta}(s), g_{\beta\alpha}(s), h_\beta(s), G_{c\alpha}(s)$
β	Zeroes of $G_{c\beta}(s)(1-\gamma(s)h_\alpha(s))$	Poles of $g_{\beta\beta}(s)$, $g_{\alpha\beta}(s), g_{\beta\alpha}(s), h_\alpha(s), G_{c\beta}(s)$

As discussed earlier, there are two resonant frequencies under the unbalanced grid impedance. For convenience, it is simplified as two simple equivalent *LCR* series resonant circuits, whose equivalent inductances are

$$L_{E1} = \frac{1}{w_{\text{res1}}^2 C}$$
$$L_{E2} = \frac{1}{w_{\text{res2}}^2 C}. \tag{25}$$

Further, the R_d can be optimized by calculating the Q-factor of the filter [36], [37], i.e.,

$$R_{d1} = \frac{1}{Q_1}\sqrt{\frac{L_{E1}}{C}}$$
$$R_{d2} = \frac{1}{Q_2}\sqrt{\frac{L_{E2}}{C}} \tag{26}$$

where Q_1 and Q_2 can be selected according to the well-established method in [36] and [37]. Thus the R_d is finally obtained

$$R_d = \frac{R_{d1} + R_{d2}}{2}. \tag{27}$$

For the strong robustness under the most severe imbalance of grid impedance, the R_d is recommended to be designed at $L_{gc} = L_{gc\max}$ when taking the gain margin and the power losses into consideration. In this article, $R_d = 5\ \Omega$ is selected.

C. Design the Proportional Gains $K_{p\alpha}$ and $K_{p\beta}$ of the PR+HC Regulators

Consider the open-loop transfer functions $T_\alpha(s)$ in (12), $T_\beta(s)$ in (13), and determine the pole-zero structures of channels α and β, respectively. Assuming that there is no pole-zero cancellation within $\gamma(s)$, it can be observed from (14) that the poles of $\gamma(s)$ are the poles of $g_{\alpha\beta}(s)$ and $g_{\beta\alpha}(s)$ and the zeroes of $g_{\alpha\alpha}(s)$ and $g_{\beta\beta}(s)$. In addition, the zeroes of $h_\beta(s)$ in (16) include the zeroes of $g_{\beta\beta}(s)$. Hence, for channel α, the zeroes of $T_\alpha(s)$ are the zeroes of $G_{c\alpha}(s)(1-\gamma(s)h_\beta(s))$ since the zeroes of $g_{\alpha\alpha}(s)$ coincide with poles of $\gamma(s)$, and the poles of $T_\alpha(s)$ are the poles of $G_{c\alpha}(s), g_{\alpha\alpha}(s), g_{\alpha\beta}(s), g_{\beta\alpha}(s)$, and $h_\beta(s)$. Channel β has a similar pole-zero structure. The open-loop zeroes and poles of both channels are summarized in Table II.

According to Fig. 9(a), the closed-loop response of channel α is given by

$$i_{g\alpha}(s) = T_{\alpha\_cl}(s)\cdot i_{\text{ref\_}g\alpha}(s) + S_\alpha(s)\cdot i_{\text{ref\_}g\beta}(s) \tag{28}$$

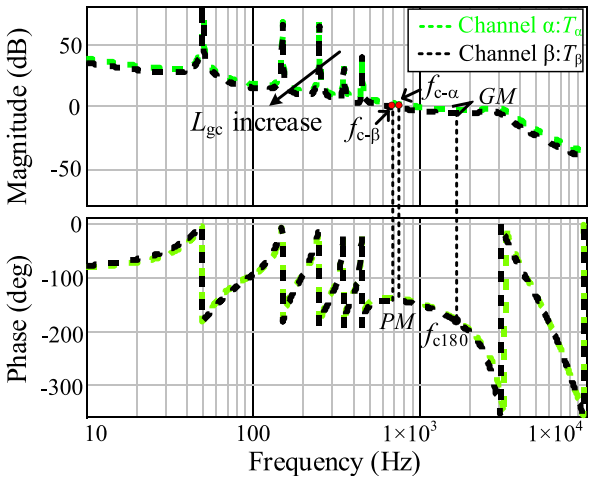

Fig. 12. Bode plots of individual channels α and β.

where

$$T_{\alpha\_cl}(s) = \frac{T_\alpha(s)}{1+T_\alpha(s)} \tag{29}$$

$$S_\alpha(s) = \frac{1}{1+T_\alpha(s)} \cdot \frac{g_{\alpha\beta}(s)}{g_{\beta\beta}(s)} \cdot h_\beta(s). \tag{30}$$

It can be obtained from Table II that the poles of $T_{\alpha\_cl}(s)$ and $S_\alpha(s)$ are the same and are the zeroes of $(1+T_\alpha(s))$, since both the poles of $T_\alpha(s)$ and the poles of $g_{\alpha\beta}(s)h_\beta(s)/g_{\beta\beta}(s)$ coincide with poles of $(1+T_\alpha(s))$. If $G_{c\alpha}(s)$ is a stable controller for channel α, and the reference signals $i_{\text{ref}\_g\alpha}(s)$ and $i_{\text{ref}\_g\beta}(s)$ are stable, then both signals to $i_{g\alpha}(s)$, $T_{\alpha\_cl}(s)i_{\text{ref}\_g\alpha}(s)$, and $S_\alpha(s)i_{\text{ref}\_g\beta}(s)$, respectively, are stable. Hence, $S_\alpha(s)i_{\text{ref}\_g\beta}(s)$ can be regarded as a normal disturbance acting on channel α.

Similarly, according to Fig. 9(b), the closed-loop response of channel β is described as

$$i_{g\beta}(s) = T_{\beta\_cl}(s) \cdot i_{\text{ref}\_g\beta}(s) + S_\beta(s) \cdot i_{\text{ref}\_g\alpha}(s) \tag{31}$$

where

$$T_{\beta\_cl}(s) = \frac{T_\beta(s)}{1+T_\beta(s)} \tag{32}$$

$$S_\beta(s) = \frac{1}{1+T_\beta(s)} \cdot \frac{g_{\beta\alpha}(s)}{g_{\alpha\alpha}(s)} \cdot h_\alpha(s). \tag{33}$$

The poles of $T_{\beta\_cl}(s)$ and $S_\beta(s)$ are the same as the zeroes of $(1+T_\beta(s))$, and $S_\beta(s)i_{\text{ref}\_g\alpha}(s)$ can likewise be treated as a normal disturbance acting on channel β.

Therefore, the global stability of control system depends only on the stability of the open-loop transfer functions $T_\alpha(s)$ and $T_\beta(s)$. Then, the classical concepts in SISO systems, such as Nyquist stability criterion, gain and phase margins, can be extended to the multivariable control system and be applied to analyze the stability and design the controller parameters, regardless of the loop interactions.

Fig. 12 shows the Bode plots of individual channels α and β of the three-phase *LCL*-filter-based grid-tied inverter with $L_{ga} = L_{gb} \neq L_{gc}$ and $G_{c\alpha}(s) = G_{c\beta}(s)$. The bandwidths of the open-loop transfer functions $T_\alpha(s)$ and $T_\beta(s)$ are different and decrease as the value of L_{gc} increases. However, when designing the controller parameters, it should make the system meet with the requirements of gain margins GM and phase margins PM as well as the bandwidths of channels α and β.

The current controller matrix $G_c(s)$ is usually simplified as $K_p(s)$ [15], since the resonance terms have a negligible influence on the stability of system, if the control bandwidth is well set. Then, the gain margins and phase margins of the channels α and β can be calculated as

$$\begin{aligned} \text{GM}_\alpha &= -20\log\left|K_{p\alpha}G_{\text{inv}}G_{\alpha\ \text{plant}}(j\omega)\right|\Big|_{\omega=2\pi f_{c180\_\alpha}} \\ \text{PM}_\alpha &= 180^\circ + \left(\angle G_{\alpha\ \text{plant}}(j\omega) - \frac{360}{2\pi f_s}\lambda\omega\right)\Big|_{\omega=2\pi f_{c\_\alpha}} \end{aligned} \tag{34}$$

$$\begin{aligned} \text{GM}_\beta &= -20\log\left|K_{p\beta}G_{\text{inv}}G_{\beta\ \text{plant}}(j\omega)\right|\Big|_{\omega=2\pi f_{c180\_\beta}} \\ \text{PM}_\beta &= 180^\circ + \left(\angle G_{\beta\ \text{plant}}(j\omega) - \frac{360}{2\pi f_s}\lambda\omega\right)\Big|_{\omega=2\pi f_{c\_\beta}} \end{aligned} \tag{35}$$

where $f_{c-\alpha}$ and $f_{c-\beta}$ are the crossover frequencies of the channels α and β; $f_{c180-\alpha}$ and $f_{c180-\beta}$ are the frequencies when the phases of the channels α and β cross -180°.

To achieve the desired control bandwidth, the minimum crossover frequencies of the channels α and β should be set higher than the highest order harmonic compensator frequency under $L_{gc} = L_{gc\max}$. Then, the minimum control gains can be calculated as

$$\begin{aligned} \left|K_{p\alpha\_\min}G_{\text{inv}}G_{\alpha\ \text{plant}}(j\omega)\right|\Big|_{\omega=2\pi f_{c\_\alpha\ \min}} &= 1 \\ \left|K_{p\beta\_\min}G_{\text{inv}}G_{\beta\ \text{plant}}(j\omega)\right|\Big|_{\omega=2\pi f_{c\_\beta\ \min}} &= 1. \end{aligned} \tag{36}$$

Simultaneously, in order to guarantee the sufficient stability margins under $L_{gc} = L_{gc\min}$, the maximum control gains should be limited as

$$\begin{aligned} K_{p\alpha\_\max} &= \min(K_{p\alpha\_\max 1}, K_{p\alpha\_\max 2}) \\ K_{p\beta\_\max} &= \min(K_{p\beta\_\max 1}, K_{p\beta\_\max 2}) \end{aligned} \tag{37}$$

where $K_{p\alpha\_\max 1}$ and $K_{p\alpha\_\max 2}$ are the controller gains that are determined by $\text{GM}_\alpha = 3$ dB, and $\text{PM}_\alpha = 30^\circ$, respectively. Similarly, $K_{p\beta\_\max 1}$ and $K_{p\beta\_\max 2}$ are the controller gains that are determined by $\text{GM}_\beta = 3$ dB and $\text{PM}_\beta = 30^\circ$, respectively. If $K_{p\alpha\_\max} < K_{p\alpha\_\min}, K_{p\beta\_\max} < K_{p\beta\_\min}$, it is necessary to cut down the desired control bandwidths until proper intervals are obtained.

It should be pointed out that each channel has GM and PM, thus there are two GMs and PMs, denoted as GM_α, GM_β, PM_α, and PM_β in the article. As a whole system, the GM and PM are defined as the smaller of the two.

D. Coupling Analysis

For channel α, the cross-coupling between individual channels, according to (30), can be fully evaluated by

$$\frac{i_{g\alpha}(s)}{i_{\text{ref}\_g\beta}(s)} = S_\alpha(s) = \frac{1}{1+T_\alpha(s)} \cdot \frac{g_{\alpha\beta}(s)}{g_{\beta\beta}(s)} \cdot h_\beta(s). \tag{38}$$

Fig. 13 presents the Bode plots of the coupling from $i_{\text{ref}\_g\beta}(s)$ to $i_{g\alpha}(s)$. It can be easily observed that the coupling magnitude increases as L_{gc} does, which means the more severe imbalance of grid impedance, the higher loop interaction, and the worst

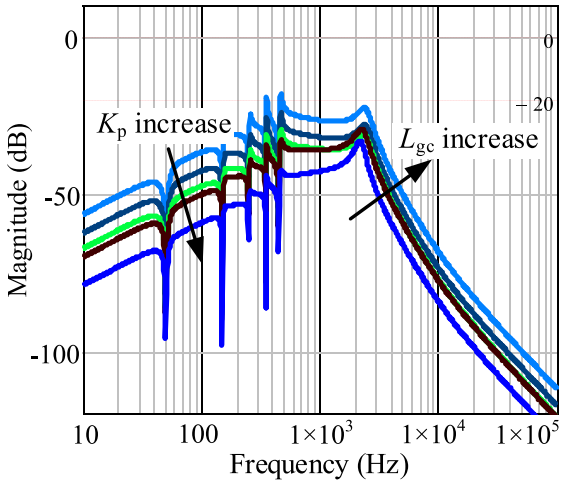

Fig. 13. Bode plot of the coupling from $i_{\mathrm{ref\_}g\beta}(s)$ to $i_{g\alpha}(s)$.

cross-coupling will occur at $L_{gc} = L_{gc\max}$. Additionally, it can also be seen that the coupling magnitude decreases as control gain $K_{p\alpha}$ increases. If a controller $G_{c\alpha}(s)$ is designed so that a high gain is achieved, this will guarantee that the cross-coupling is significantly low. Therefore, a conclusion can be drawn that a controller $G_{c\alpha}(s)$ offering a high gain tends to reduce the coupling effect introduced by the unbalanced grid impedance. A proper $K_{p\alpha}$ can ensure that the coupling magnitude is much less than -20 dB, especially at the low frequency range and the *h*-order harmonic, meaning that the coupling is virtually nonexistent. The observations are similar when analyzing the coupling of the channel β.

V. Design Methods Comparison

In this section, the two analysis and design methods are compared under the unbalanced grid impedance, which is assumed as $L_{ga} = L_{gb} = 4$ mH, $L_{gc} = 8$ mH. Both methods are analyzed in the stationary $\alpha\beta\gamma$ frame. Consider the following representations.

1) Method A: Directly neglecting the coupling terms $g_{\alpha\beta}(s)$ and $g_{\beta\alpha}(s)$ defined in (5) when tuning current controller parameters.
2) Method B: The proposed method with no loss of the structural information.

Here, $T_{\alpha-i}(s)$ ($i =$ A and B) are defined to denote the α-axis open-loop transfer functions of methods *i*. Similarly, $T_{\beta-i}(s)$ are defined to denote the β-axis open-loop transfer functions of methods *i*. Additionally, $K_{p\alpha-i}$ and $K_{p\beta-i}$ are proportional gains of α- and β-axes current controllers, respectively.

To figure out the stable regions, the Nyquist diagrams of $T_{\alpha-i}(s)$ and $T_{\beta-i}(s)$ are utilized. As well known, the Nyquist trajectory will cross point $(-1, 0)$ when the critical gain is adopted. Thus, the stable regions of the two methods can be summarized in Table III.

It can be easily concluded from Table III that the different stability regions are figured out when the two analysis and design methods are adopted under unbalanced grid impedance with

TABLE III
Stable Region Analysis

Method	Stable Region
A	$K_{p\alpha\text{-A}}$ <1.78, $K_{p\beta\text{-A}}$ <1.91
B	$K_{p\alpha\text{-B}}$ <1.63, $K_{p\beta\text{-B}}$ <1.74

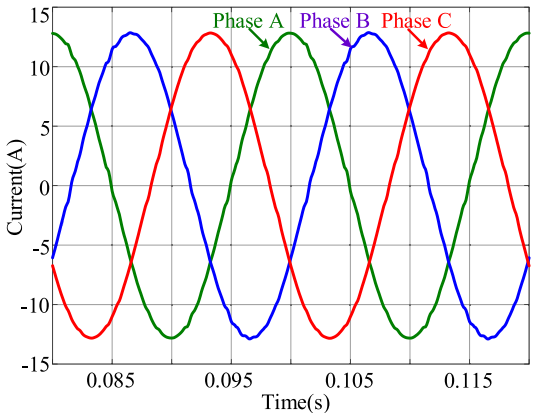

Fig. 14. Simulated waveform of the grid-injected current with $K_{p\alpha} = 1.60$, $K_{p\beta} = 1.70$ and $L_{ga} = L_{gb} = 4$ mH, $L_{gc} = 8$ mH.

$L_{ga} = L_{gb} = 4$ mH, $L_{gc} = 8$ mH. Compared with the Method B (the proposed method), Method A has expanded the stable region. To verify the theoretical analysis above, two sets of proportional gains are selected as follows:

i) $K_{p\alpha} = 1.60$, $K_{p\beta} = 1.70$;
ii) $K_{p\alpha} = 1.70$, $K_{p\beta} = 1.80$.

According to Table III, when (i) is adopted, Methods A and B predict that the system will be stable. And when (ii) is adopted, Method A infers the system will keep stable, contrary to what Method B deduces. The two cases will be validated by the simulation and experimental results, to demonstrate the effectiveness and accuracy of the Method B.

VI. Simulation and Experimental Verification

A. Simulation Verification

In order to verify the theoretical analysis, simulation tests on a 220 V/50 Hz/6 kW grid-tied inverter with *LCL* filter are carried out in MATLAB/Simulink, where the parameters are listed in Table I. The SPWM is adopted to generate the drive signals for the switches, and $G_{\mathrm{inv}}(s) = 35$.

To highlight the significant advantage of the proposed method over the traditional design method, the stable regions summarized in Table III have been tested under $L_{ga} = L_{gb} = 4$ mH and $L_{gc} = 8$ mH. First, the proportional gain (i) $K_{p\alpha} = 1.60$ and $K_{p\beta} = 1.70$ is utilized. The simulated grid-injected current in Fig. 14 shows that the system operates stably, which agrees with the expectations of Methods A and B. Then, the proportional gain (ii) $K_{p\alpha} = 1.70$ and $K_{p\beta} = 1.80$ is adopted. The corresponding result of the grid-injected current is presented in Fig. 15. Evidently, the system oscillates seriously, which is

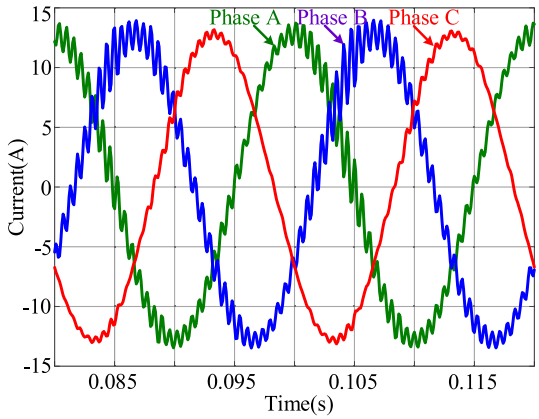

Fig. 15. The simulated waveform of the grid-injected current with $K_{p\alpha} = 1.70$, $K_{p\beta} = 1.80$, and $L_{ga} = L_{gb} = 4\,\text{mH}$, $L_{gc} = 8\,\text{mH}$.

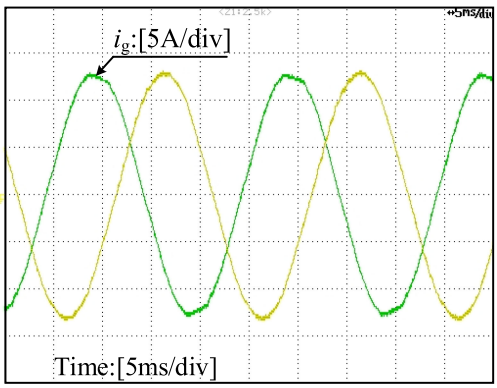

Fig. 16. Grid-injected current with $K_{p\alpha} = 1.60$, $K_{p\beta} = 1.70$ and $L_{ga} = L_{gb} = 4\,\text{mH}$, $L_{gc} = 8\,\text{mH}$.

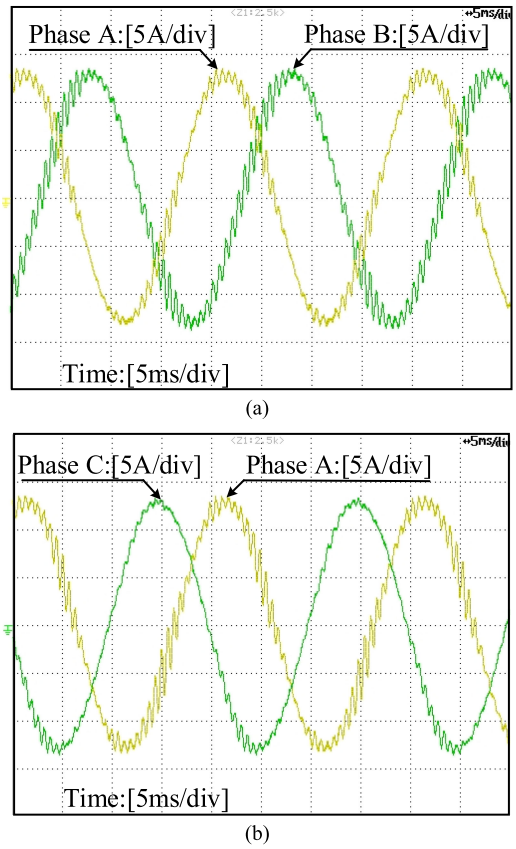

Fig. 17. Grid-injected current with $K_{p\alpha} = 1.70$, $K_{p\beta} = 1.80$ and $L_{ga} = L_{gb} = 4\,\text{mH}$, $L_{gc} = 8\,\text{mH}$. (a) Phases A and B. (b) Phases A and C.

consistent with the prediction of Method B, while contrary to what the Method A infers. Thus, Method A cannot provide precise stability analysis when grid impedance is unbalanced. In addition, by comparing Method A with Method B, it can be obtained that when analyzing the stability and tuning the controller parameters, directly neglecting the coupling terms will lead to imprecise results.

B. Experimental Verification

In order to further confirm the effectiveness of proposed method, a 220 V/50 Hz/6 kW grid-tied inverter with *LCL* filter prototype is constructed based on the dSPACE DS 1202. The experimental parameters coincide with those utilized in simulations. To emulate the unbalanced grid impedance, the external inductors are utilized.

To validate the accuracy of the proposed analysis method under unbalanced grid impedance ($L_{ga} = L_{gb} = 4$ mH, and $L_{gc} = 8$ mH), the different proportional gains (i) $K_{p\alpha} = 1.60$, $K_{p\beta} = 1.70$ and (ii) $K_{p\alpha} = 1.70$, $K_{p\beta} = 1.80$ are adopted on the basis of previous analysis. Fig. 16 presents the waveform of the grid-injected current when (i) $K_{p\alpha} = 1.60$ and $K_{p\beta} = 1.70$ is utilized for current controllers. It is obvious that the system can remain stable, which matches what the Methods A and B have predicted. Furthermore, Fig. 17(a) and (b) shows the waveforms of the grid-injected currents when (ii) $K_{p\alpha} = 1.70$ and $K_{p\beta} = 1.80$ is used. It can be observed that the severe oscillation arises in the grid-injected current, which indicates instability and fully verifies the theoretical expectation of the Method B (the proposed method). Thus, a conclusion can be drawn that, compared with the conventional method (Method A), the proposed method can provide more precise stability analysis under the unbalanced grid impedance, since there is no assumption or loss of multivariable information when deriving the equivalent individual channel representation.

VII. Discussion

From the simulation and experimental results, it can be observed that these are identical to the previous theoretical analysis. In addition, the following findings still need to be highlighted.

A. Comparison With the GNC

As a contrast, the GNC is applied for analyzing the stability under the unbalanced grid impedance with $L_{ga} = L_{gb} = 4\,\text{mH}$, $L_{gc} = 8\,\text{mH}$. According to Fig. 7, the return-ratio matrix $L(s)$

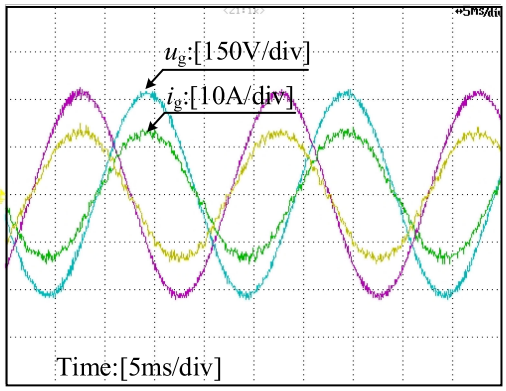

Fig. 18. Experimental waveform when the system is critically stable with $K_{p\alpha} = 1.63$, $K_{p\beta} = 1.74$ and $L_{ga} = L_{gb} = 4$ mH, $L_{gc} = 8$ mH.

can be expressed as

$$L(s) = \begin{pmatrix} g_{\alpha\alpha}(s) & g_{\alpha\beta}(s) \\ g_{\beta\alpha}(s) & g_{\beta\beta}(s) \end{pmatrix} \times \begin{pmatrix} G_{c\alpha}(s)G_{\mathrm{del}}(s)G_{\mathrm{inv}}(s) & \\ & G_{c\beta}(s)G_{\mathrm{del}}(s)G_{\mathrm{inv}}(s) \end{pmatrix}. \tag{39}$$

Then, the eigenvalues of $L(s)$ can be calculated as below

$$|\lambda_{1,2}(s)I_2 - L(s)| = 0 \tag{40}$$

where $\lambda_{1,2}(s)$ are the eigenvalues of $L(s)$. Obviously, there are two PMs and GMs, as well. Again, the PM and GM are defined as the smaller of the two when applying the GNC to eigenvalues of $L(s)$.

According to GNC, the eigenvalues $\lambda_{1,2}(s)$ can be utilized to analyze the stability [20], [38]. If the Nyquist trajectories of $\lambda_{1,2}(s)$ do not encircle the critical point $(-1, 0)$, the system is stable. Therefore, the stable region deduced by GNC can be obtained as $K_{p\alpha-C} < 1.63$ and $K_{p\beta-C} < 1.74$, which is consistent with the proposed method. To verify the accuracy of the proposed method and GNC, the third set of the proportional gains is selected as

iii) $K_{p\alpha} = 1.63$, $K_{p\beta} = 1.74$.

Apparently, when (iii) $K_{p\alpha} = 1.63$ and $K_{p\beta} = 1.74$ are utilized, the proposed method and GNC predict that the system is critically stable. Fig. 18 shows the corresponding experimental waveform, which fully matches with the expectations of proposed method and GNC. Therefore, the proposed method is as accurate as the GNC, and both of them can precisely analyze the stability of the three-phase grid-tied inverter with *LCL* filter under unbalanced grid impedance. However, it is worth highlighting the superiority of the proposed method over the GNC in the stability analysis and controller parameters tuning.

1) It is simpler to figure out the stability regions by adopting the proposed method. As proved in Section IV-C, the global stability of control system depends only on the stability of the open-loop transfer functions Tα(s) and Tβ(s). Thus, the stability regions of α- and β-axes can be easily calculated out according to PM$\alpha\beta = 0$ or GM$\alpha\beta = 0$. However, The GNC needs to repeatedly utilize the trial-and-error method to adjust the controller gains $K_{p\alpha}$ and $K_{p\beta}$ until the Nyquist trajectories of $\lambda_{1,2}$(s) cross the critical point $(-1, 0)$. This process is time-consuming and brings the high computational effort.
2) It is easier to determine the optimal controller parameters by utilizing the proposed method. According to Fig. 12, due to the unbalanced grid impedance, there exist significant differences between the characteristics of α- and β-axes. By independently tuning the controller parameters according to the proposed method, the gain and phase margins as well as the bandwidths of α- and β-axes are almost equal under unbalanced grid impedance, as depicted in Fig. 19. Thus, the optimal parameters can be tuned and the effect of the differences between the characteristics of α- and β-axes on the control performance can be effectively attenuated.

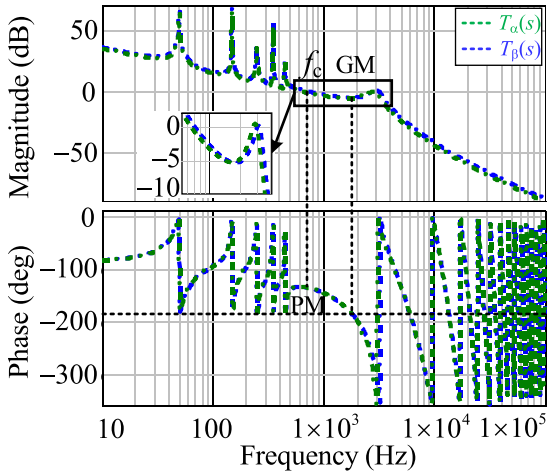

Fig. 19. Bode plots of $T_\alpha(s)$ and $T_\beta(s)$ with $K_{p\alpha-B} = 1.20$, $K_{p\beta-B} = 1.32$ under $L_{ga} = L_{gb} = 4$ mH, $L_{gc} = 8$ mH.

While, the GNC cannot provide the open-loop transfer functions $T_\alpha(s)$ and $T_\beta(s)$, thus the gain and phase margins as well as the bandwidths of α- and β-axes are unknown. Although the gains $K_{p\alpha}$ and $K_{p\beta}$ can be determined according to the *PM* and *GM* of $\lambda_{1,2}(s)$, it is complicated to judge whether $K_{p\alpha}$ and $K_{p\beta}$ are optimal or not. For simplicity, in the existing method, for example in [20], the current controllers of the α- and β-axes are selected as the same, i.e., $G_{c\alpha}(s) = G_{c\beta}(s)$. However, this affects the control performance, which will be demonstrated in next part.

B. Comparison With the Existing Method Whose Controllers of α- and β-Axes Are Designed as the Same

In existing control strategy, the current controllers $G_{c\alpha}(s)$ and $G_{c\beta}(s)$ are generally selected as the same, no matter the grid impedance is balanced or not. However, according to Fig. 12, under the unbalanced grid impedance, when $G_{c\alpha}(s) = G_{c\beta}(s)$, the characteristics of the open-loop transfer functions $T_\alpha(s)$ and $T_\beta(s)$ are evidently different, which may bring adverse effect on the control performance. In this scenario, the comparison between the existing method with $G_{c\alpha}(s) = G_{c\beta}(s)$ (Method

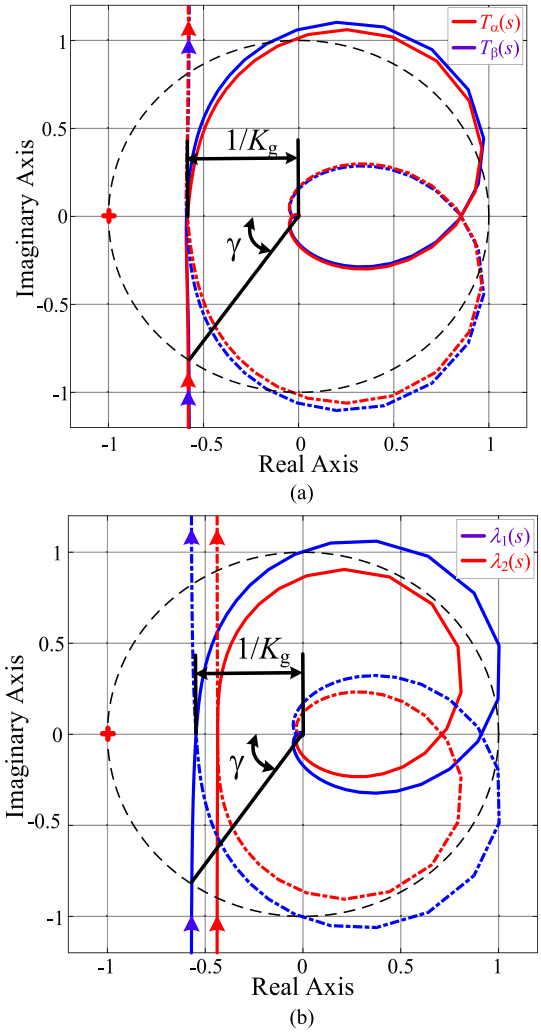

Fig. 20. Nyquist plots of $T_\alpha(s)$, $T_\beta(s)$, and $\lambda_{1,2}(s)$ under $L_{ga} = L_{gb} = 4$ mH, $L_{gc} = 8$ mH. (a) Nyquist plots of $T_\alpha(s)$, $T_\beta(s)$ with $K_{p\alpha-B} = 1.20$, $K_{p\beta-B} = 1.32$ in Method B. (b) Nyquist plots of $\lambda_{1,2}(s)$ with $K_{p\alpha-C} = 1.22$, $K_{p\beta-C} = 1.22$ in Method C.

C) is proposed in [20] and the proposed strategy has been carried out.

As mentioned before, in this article, there exist two GMs and PMs, denoted as GM_α, GM_β, PM_α, and PM_β, respectively. It is worth noting that, by tuning independently current controllers of channels α and β according to the proposed strategy, GM_α can be equal approximately to GM_β and PM_α can be equal approximately to PM_β. Fig. 19 depicts the Bode plots of $T_\alpha(s)$ and $T_\beta(s)$ with $K_{p\alpha-B} = 1.20$, $K_{p\beta-B} = 1.32$ under $L_{ga} = L_{gb} = 4$ mH, $L_{gc} = 8$ mH. It can be found that the gain margins and phase margins as well as the bandwidths of channels α and β are almost equal, while Method C cannot do the same. To evaluate the performance under the proposed strategy (Method B) and Method C, more tests have been conducted.

Fig. 20(a) and (b) depict the Nyquist trajectories of $T_\alpha(s)$ and $T_\beta(s)$ with $K_{p\alpha-B} = 1.20$ and $K_{p\beta-B} = 1.32$ in Method B and Nyquist trajectories of $\lambda_{1,2}(s)$ with $K_{p\alpha-C} = 1.22$ and $K_{p\beta-C} = 1.22$ in Method C. It can be observed that the gain margins GM, as well as the phase margins PM, are equal under

TABLE IV
PERFORMANCE COMPARISON

Method	THD		
	Phase A	Phase B	Phase C
B	1.42%	1.35%	1.20%
C	1.54%	1.69%	1.32%

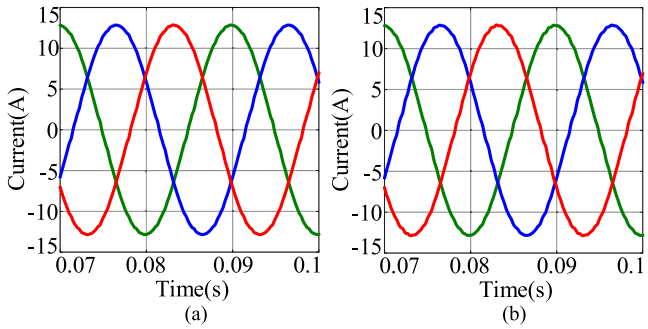

Fig. 21. Simulated waveform of the grid-injected current with $L_{ga} = L_{gb} = 4$ mH, $L_{gc} = 8$ mH. (a) Under nominal condition. (b) Under parameter variation condition.

both methods. Therefore, a fair performance comparison can be made. Table IV summarizes the total harmonic distortion (THD) of the each-phase grid-injected current. Apparently, the proposed method can achieve better control performance. That can be explained as follows: according to Fig. 12, when $G_{c\alpha}(s) = G_{c\beta}(s)$ in the Method C, the bandwidth and gain in the low frequency segment of $T_\beta(s)$ are decayed compared with $T_\alpha(s)$, which finally reduces the ability to reject the low-frequency harmonics, while the Method B has overcome this issue owing to the same bandwidths of $T_\alpha(s)$ and $T_\beta(s)$. It should be pointed out that the more severe the imbalance of the grid impedance, the more significant the difference between the characteristics of $T_\alpha(s)$ and $T_\beta(s)$ is. Thus, in the applications under severely unbalanced grid impedance, it is highly recommended to adopt the proposed method to analyze the stability and tune the controller parameters.

C. Evaluation of the Structural Robustness Under the Unbalanced Grid Impedance

As depicted in Fig. 10, the greater the value of L_{gc}, the closer the trajectory of $\gamma(s)$ is to (1, 0). To assess the structural robustness when $\gamma(s)$ crosses near (1, 0), the sensitivity to parameter uncertainty is evaluated under two cases:

I) $L_{ga} = L_{gb} = 4$ mH, $L_{gc} = 8$ mH;
II) $L_{ga} = L_{gb} = 4$ mH, $L_{gc} = 20$ mH.

Obviously, the Nyquist trajectory of $\gamma(s)$ under (II) is closer to (1, 0) than that under case (I), thus the case (II) is expected to be more sensitive to parameter uncertainty.

Fig. 21 presents the simulation results both under nominal condition and parameter variation of +30% in L_1, +20% in C and +30% in L_2 when the case (I) with $R_d = 0\ \Omega$ is evaluated. It is easily observed that robustness can be guaranteed. As a

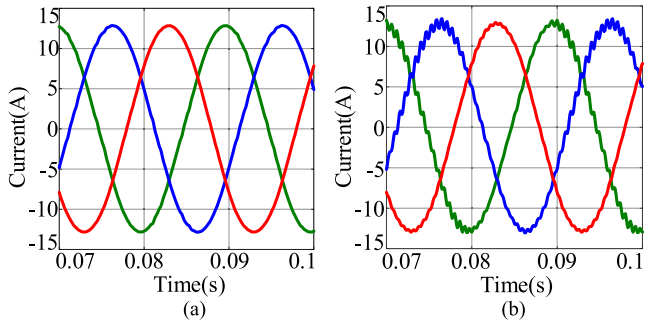

Fig. 22. Simulated waveform of the grid-injected current with $L_{ga} = L_{gb} =$ 4 mH, $L_{gc} = 20$ mH. (a) Under nominal condition. (b) Under parameter variation condition.

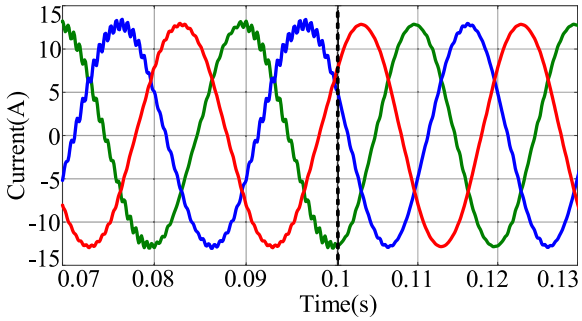

Fig. 23. Simulated waveform of the grid-injected current with $L_{ga} = L_{gb} =$ 4 mH, $L_{gc} = 20$ mH under parameter variation condition when $R_d = 5\ \Omega$ is adopted at $t = 0.1$ s.

contrast, when the case (II) with $R_d = 0\ \Omega$ is assessed, the simulation results both under nominal condition and parameter variation of $+30\%$ in L_1, $+20\%$ in C and $+30\%$ in L_2 are shown in Fig. 22. From Fig. 22(a) to (b), the system becomes unstable, indicating that it is sensitive to parameter uncertainty, which verifies the theoretical analysis.

Further, according to Fig. 11, the passive damper R_d can improve the robustness. To confirm that, $R_d = 5\ \Omega$ is inserted. Fig. 23 shows the simulated waveform of the grid-injected current with $L_{ga} = L_{gb} = 4$ mH and $L_{gc} = 20$ mH under parameter variation condition when $R_d = 5\ \Omega$ is adopted at $t = 0.1$ s. It is clear that the sensitivity issue has been relaxed owing to R_d, which completely matches with the theoretical analysis.

VIII. Conclusion

This article proposes a precise stability analysis and controller design method based on ICAD for three-phase grid-tied inverter with *LCL* filter under unbalanced grid impedance. The principle of the proposed method is deduced in detail. According to the theoretical analysis, the following conclusions can be drawn.

1) When analyzing the stability and tuning the controller, directly neglecting the cross-coupling will lead to imprecise results. Compared with the traditional method that neglects the coupling, the proposed method can provide more precise stability analysis under unbalanced grid impedance, since there is no loss of structural information when deriving the equivalent individual channel representation.
2) By using ICAD, the highly coupled MIMO system can be decomposed into SISO subsystems, where Bode/Nyquist techniques can be applied. Thus, the stability analysis and controller design under unbalanced grid impedance have been simplified.
3) By independently tuning the current controller parameters, the better control performance can be achieved, since the gain and phase margins as well as the bandwidths of α- and β-axes are almost equal under the unbalanced grid impedance.
4) The unbalanced grid impedance deteriorates the structural robustness. And the more severe the imbalance of grid impedance, the poorer structural robustness is. The passive damping can significantly enhance the structural robustness.

Simulations and experiments on a 220 V/50 Hz/6 kW *LCL*-filter-based three-phase grid-tied inverter prototype have fully verified the effectiveness and accuracy of the proposed method.

Appendix

$$Z_1 = L_1 s,\ Z_2 = (CR_d s + 1)/(Cs),\ Z_3 = L_2 s$$
$$Z_{Lga} = sL_{ga},\ Z_{Lgb} = sL_{gb},\ Z_{Lgc} = sL_{gc} \tag{A1.1}$$
$$\begin{aligned}\Delta_1 &= 3Z_1^2Z_2^2 + 3Z_1^2Z_3^2 + 3Z_2^2Z_3^2 \\ &\quad + 6Z_1Z_2Z_3^2 + 6Z_1Z_2^2Z_3 + 6Z_1^2Z_2Z_3 \\ \Delta_2 &= (Z_1^2 + Z_2^2 + 2Z_1Z_2) \\ &\quad \cdot (Z_{Lga}Z_{Lgb} + Z_{Lga}Z_{Lgc} + Z_{Lgb}Z_{Lgc}) \\ \Delta_3 &= 2(Z_{Lga} + Z_{Lgb} + Z_{Lgc}) \\ &\quad \cdot (Z_1Z_2^2 + Z_1^2Z_2 + Z_1^2Z_3 + Z_2^2Z_3 + 2Z_1Z_2Z_3)\end{aligned} \tag{A1.2}$$
$$\begin{aligned}Y_{12} = Y_{21} &= -Z_2(Z_1Z_2 + Z_2Z_3 + Z_1Z_3 + Z_1Z_{Lgc} \\ &\quad + Z_2Z_{Lgc})/(\Delta_1 + \Delta_2 + \Delta_3) \\ Y_{13} = Y_{31} &= -Z_2(Z_1Z_2 + Z_2Z_3 + Z_1Z_3 + Z_1Z_{Lgb} \\ &\quad + Z_2Z_{Lgb})/(\Delta_1 + \Delta_2 + \Delta_3) \\ Y_{23} = Y_{32} &= -Z_2(Z_1Z_2 + Z_2Z_3 + Z_1Z_3 + Z_1Z_{Lga} \\ &\quad + Z_2Z_{Lga})/(\Delta_1 + \Delta_2 + \Delta_3) \\ Y_{11} &= Z_2(2Z_1Z_2 + 2Z_2Z_3 + 2Z_1Z_3 + (Z_1 + Z_2) \\ &\quad \times (Z_{Lgb} + Z_{Lgc}))/(\Delta_1 + \Delta_2 + \Delta_3) \\ Y_{22} &= Z_2(2Z_1Z_2 + 2Z_2Z_3 + 2Z_1Z_3 + (Z_1 + Z_2) \\ &\quad \times (Z_{Lga} + Z_{Lgc}))/(\Delta_1 + \Delta_2 + \Delta_3) \\ Y_{33} &= Z_2(2Z_1Z_2 + 2Z_2Z_3 + 2Z_1Z_3 + (Z_1 + Z_2) \\ &\quad \times (Z_{Lga} + Z_{Lgb}))/(\Delta_1 + \Delta_2 + \Delta_3)\end{aligned} \tag{A1.3}$$

$$
\begin{aligned}
g_{\alpha\alpha} &= \frac{2(2Y_{11}-Y_{12}-Y_{13})-2Y_{21}+Y_{22}+Y_{23}}{-2Y_{31}+Y_{32}+Y_{33}}{6} \\
g_{\alpha\beta} &= \frac{\sqrt{3}(Y_{23}-2Y_{13}+Y_{33}-Y_{22}+2Y_{12}-Y_{32})}{6} \\
g_{\beta\alpha} &= \frac{\sqrt{3}(2Y_{21}-2Y_{31}-Y_{22}+Y_{32}-Y_{23}+Y_{33})}{6} \\
g_{\beta\beta} &= \frac{Y_{22}-Y_{23}-Y_{32}+Y_{33}}{2}
\end{aligned} \tag{A1.4}
$$

REFERENCES

[1] M. Lu, A. Al-Durra, S. M. Muyeen, S. Leng, P. C. Loh, and F. Blaabjerg, "Benchmarking of stability and robustness against grid impedance variation for *LCL*-filtered grid-interfacing inverters," *IEEE Trans. Power Electron.*, vol. 33, no. 10, pp. 9033–9046, Oct. 2018.

[2] W. Wu, Y. Liu, Y. He, H. S. Chung, M. Liserre, and F. Blaabjerg, "Damping methods for resonances caused by *LCL*-filter-based current-controlled grid-tied power inverters: An overview," *IEEE Trans. Ind. Electron.*, vol. 64, no. 9, pp. 7402–7413, Sep. 2017.

[3] R. A. Fantino, C. A. Busada, and J. A. Solsona, "Observer-based grid-voltage sensorless synchronization and control of a VSI-*LCL* tied to an unbalanced grid," *IEEE Trans. Ind. Electron.*, vol. 66, no. 7, pp. 4972–4981, Jul. 2019.

[4] R. Guzman, L. G. de Vicuña, M. Castilla, J. Miret, and J. de la Hoz, "Variable structure control for three-phase *LCL*-filtered inverters using a reduced converter model," *IEEE Trans. Ind. Electron.*, vol. 65, no. 1, pp. 5–15, Jan. 2018.

[5] T. Wu, M. Misra, Y. Jhang, Y. Huang, and L. Lin, "Direct digital control of single-phase grid-connected inverters with *LCL* filter based on inductance estimation model," *IEEE Trans. Power Electron.*, vol. 34, no. 2, pp. 1851–1862, Feb. 2019.

[6] R. N. Beres, X. Wang, F. Blaabjerg, M. Liserre, and C. L. Bak, "Optimal design of high-order passive-damped filters for grid-connected applications," *IEEE Trans. Power Electron.*, vol. 31, no. 3, pp. 2083–2098, Mar. 2016.

[7] E. Rodriguez-Diaz, F. D. Freijedo, J. C. Vasquez, and J. M. Guerrero, "Analysis and comparison of notch filter and capacitor voltage feedforward active damping techniques for *LCL* grid-connected converters," *IEEE Trans. Power Electron.*, vol. 34, no. 4, pp. 3958–3972, Apr. 2019.

[8] J. Ye, A. Shen, Z. Zhang, J. Xu, and F. Wu, "Systematic design of the hybrid damping method for three-phase inverters with high-order filters," *IEEE Trans. Power Electron.*, vol. 33, no. 6, pp. 4944–4956, Jun. 2018.

[9] X. Li, J. Fang, Y. Tang, X. Wu, and Y. Geng, "Capacitor-voltage feedforward with full delay compensation to improve weak grids adaptability of *LCL*-filtered grid-connected converters for distributed generation systems," *IEEE Trans. Power Electron.*, vol. 33, no. 1, pp. 749–764, Jan. 2018.

[10] X. Li, J. Fang, Y. Tang, and X. Wu, "Robust design of *LCL* filters for single-current-loop-controlled grid-tied power converters with unit PCC voltage feedforward," *IEEE J. Emerg. Sel. Topics Power Electron.*, vol. 6, no. 1, pp. 54–72, Mar. 2018.

[11] X. Zhou *et al.*, "Robust grid-current-feedback resonance suppression method for *LCL*-type grid-connected inverter connected to weak grid," *IEEE J. Emerg. Sel. Topics Power Electron.*, vol. 6, no. 4, pp. 2126–2137, Dec. 2018.

[12] L. Zhou *et al.*, "Inverter-current-feedback resonance-suppression method for *LCL*-type DG system to reduce resonance-frequency offset and grid-inductance effect," *IEEE Trans. Ind. Electron.*, vol. 65, no. 9, pp. 7036–7048, Sep. 2018.

[13] Y. He, H. S. Chung, C. Lai, X. Zhang, and W. Wu, "Active cancelation of equivalent grid impedance for improving stability and injected power quality of grid-connected inverter under variable grid condition," *IEEE Trans. Power Electron.*, vol. 33, no. 11, pp. 9387–9398, Nov. 2018.

[14] D. Pan, X. Ruan, C. Bao, W. Li, and X. Wang, "Optimized controller design for *LCL*-type grid-connected inverter to achieve high robustness against grid-impedance variation," *IEEE Trans. Ind. Electron.*, vol. 62, no. 3, pp. 1537–1547, Mar. 2015.

[15] Y. Liu, W. Wu, Y. He, Z. Lin, F. Blaabjerg, and H. S. H. Chung, "An efficient and robust hybrid damper for *LCL*- or *LLCL*-based grid-tied inverter with strong grid-side harmonic voltage effect rejection," *IEEE Trans. Ind. Electron.*, vol. 63, no. 2, pp. 926–936, Feb. 2016.

[16] M. Ben Saïd-Romdhane, M. W. Naouar, I. Slama-Belkhodja, and E. Monmasson, "Robust active damping methods for *LCL* filter-based grid-connected converters," *IEEE Trans. Power Electron.*, vol. 32, no. 9, pp. 6739–6750, Sep. 2017.

[17] M. S. Sadabadi, A. Haddadi, H. Karimi, and A. Karimi, "A robust active damping control strategy for an *LCL*-based grid-connected DG unit," *IEEE Trans. Ind. Electron.*, vol. 64, no. 10, pp. 8055–8065, Oct. 2017.

[18] A. Adib, B. Mirafzal, X. Wang, and F. Blaabjerg, "On stability of voltage source inverters in weak grids," *IEEE Access*, vol. 6, pp. 4427–4439, 2018.

[19] M. Céspedes and J. Sun, "Methods for stability analysis of unbalanced three-phase systems," in *Proc. IEEE Energy Convers. Congr. Expo.*, Sep. 2012, pp. 3090–3097.

[20] W. Liu, X. Wang, and F. Blaabjerg, "Modeling of unbalanced three-phase grid-connected converters with decoupled transfer functions," in *Proc. IEEE Energy Convers. Congr. Expo.*, 2018, pp. 3164–3169.

[21] W. Jin, Y. Li, G. Sun, X. Chen, and Y. Gao, "Stability analysis method for three-phase multi-functional grid-connected inverters with unbalanced local loads considering the active imbalance compensation," *IEEE Access*, vol. 6, pp. 54865–54875, 2018.

[22] J. L. Agorreta, M. Borrega, J. López, and L. Marroyo, "Modeling and control of N-paralleled grid-connected inverters with *LCL* filter coupled due to grid impedance in PV plants," *IEEE Trans. Power Electron.*, vol. 26, no. 3, pp. 770–785, Mar. 2011.

[23] W. Li, X. Ruan, D. Pan, and X. Wang, "Full-feedforward schemes of grid voltages for a three-phase *LCL*-type grid-connected inverter," *IEEE Trans. Ind. Electron.*, vol. 60, no. 6, pp. 2237–2250, Jun. 2013.

[24] D. Pan, X. Ruan, X. Wang, F. Blaabjerg, X. Wang, and Q. Zhou, "A highly robust single-loop current control scheme for grid-connected inverter with an improved *LCCL* filter configuration," *IEEE Trans. Power Electron.*, vol. 33, no. 10, pp. 8474–8487, Oct. 2018.

[25] A. Egea-Alvarez, S. Fekriasl, F. Hassan, and O. Gomis-Bellmunt, "Advanced vector control for voltage source converters connected to weak grids," *IEEE Trans. Power Syst.*, vol. 30, no. 6, pp. 3072–3081, Nov. 2015.

[26] M. S. Sadabadi, A. Haddadi, H. Karimi, and A. Karimi, "A robust active damping control strategy for an *LCL*-based grid-connected DG unit," *IEEE Trans. Ind. Electron.*, vol. 64, no. 10, pp. 8055–8065, Oct. 2017.

[27] M. Davari and Y. A. I. Mohamed, "Robust vector control of a very weak-grid-connected voltage-source converter considering the phase-locked loop dynamics," *IEEE Trans. Power Electron.*, vol. 32, no. 2, pp. 977–994, Feb. 2017.

[28] X. Wang, F. Blaabjerg, and W. Wu, "Modeling and analysis of harmonic stability in an AC power-electronics-based power system," *IEEE Trans. Power Electron.*, vol. 29, no. 12, pp. 6421–6432, Dec. 2014.

[29] M. Huang, X. Wang, P. C. Loh, and F. Blaabjerg, "*LLCL*-filtered grid converter with improved stability and robustness," *IEEE Trans. Power Electron.*, vol. 31, no. 5, pp. 3958–3967, May 2016.

[30] J. O'Reilly and W. E. Leithead, "Multivariable control by 'individual channel design'," *Int. J. Control*, vol. 54, no. 1, pp. 1–46, 1991.

[31] D. Wang, L. Liang, J. Hu, N. Chang, and Y. Hou, "Analysis of low-frequency stability in grid-tied DFIGs by nonminimum phase zero identification," *IEEE Trans. Energy Convers.*, vol. 33, no. 2, pp. 716–729, Jun. 2018.

[32] C. E. Ugalde-Loo, E. Acha, and E. Licéaga-Castro, "Analysis of the damping characteristics of two power electronics-based devices using 'individual channel analysis and design'," *Appl. Math. Model.*, vol. 59, pp. 527–545, Feb. 2018.

[33] L. A. Amézquita-Brooks, C. E. Ugalde-Loo, E. Licéaga-Castro, and J. Licéaga-Castro, "In-depth cross-coupling analysis in high-performance induction motor control," *J. Franklin Inst.*, vol. 355, no. 5, pp. 2142–2178, 2018.

[34] L. A. Amézquita-Brooks, J. Licéaga-Castro, E. Licéaga-Castro, and C. E. Ugalde-Loo, "Induction motor control: Multivariable analysis and effective decentralized control of stator currents for high-performance applications," *IEEE Trans. Ind. Electron.*, vol. 62, no. 11, pp. 6818–6832, Nov. 2015.

[35] C. E. Ugalde-Loo, E. Acha, and E. Liceaga-Castro, "Fundamental analysis of the electromechanical oscillation damping control loop of the static VAr compensator using individual channel analysis and design," *IEEE Trans. Power Del.*, vol. 25, no. 4, pp. 3053–3069, Oct. 2010.

[36] W. Wu *et al.*, "A robust passive damping method for *LLCL*-filter-based grid-tied inverters to minimize the effect of grid harmonic voltages," *IEEE Trans. Power Electron.*, vol. 29, no. 7, pp. 3279–3289, Jul. 2014.
[37] W. Wu, Y. He, T. Tang, and F. Blaabjerg, "A new design method for the passive damped *LCL* and *LLCL* filter-based single-phase grid-tied inverter," *IEEE Trans. Ind. Electron.*, vol. 60, no. 10, pp. 4339–4350, Oct. 2013.
[38] M. Kazem Bakhshizadeh *et al.*, "Couplings in phase domain impedance modeling of grid-connected converters," *IEEE Trans. Power Electron.*, vol. 31, no. 10, pp. 6792–6796, Oct. 2016.

Weimin Wu (M'16) received the Ph.D. degrees in electrical engineering from the College of Electrical Engineering, Zhejiang University, Hangzhou, China, in 2005.

Since July 2006, he has been a Faculty Member with Shanghai Maritime University, Shanghai, China, where he is currently a Full Professor with the Department of Electrical Engineering. He worked as a Research Engineer with the Delta Power Electronic Center, Shanghai, China, from July 2005 to June 2006. He was a Visiting Professor in the Center for Power Electronics Systems, Virginia Polytechnic Institute, and State University, Blacksburg, USA, from September 2008 to March 2009. From November 2011 to January 2014, he was also a Visiting Professor with the Department of Energy Technology, Aalborg University, Demark, working at the Center of Reliable Power Electronics. He has coauthored over 100 papers and holds eight patents. His research interests include power converters for renewable energy systems, power quality, smart grid, and energy storage technology.

Dr. Wu serves as an Associate Editor for the IEEE TRANSACTIONS ON INDUSTRY ELECTRONICS.

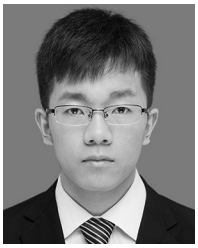

Jiahao Liu was born in Henan Province, China, in 1993. He received the B.S. degree in electrical engineering from Henan University of Science and Technology, Henan, China, in 2017. He is currently working toward the M.S. degree in electrical engineering with Shanghai Maritime University, Shanghai, China.

His current research interests include digital control techniques of power converters and renewable energy generation system.

Yun Li was born in Jiangsu Province, China, in 1990. He received the M.S. degree in electrical engineering from Shanghai Maritime University, Shanghai, China, in 2019.

He is currently with HiTrend Technology, Co., Ltd., Shanghai, China. His current research interests include smart three-phase and single-phase energy metering IC with high-precision electrical parameters and harmonic analysis.

Frede Blaabjerg (S'86–M'88–SM'97–F'03) received the Ph.D. degree in electrical engineering from Aalborg University, Aalborg, Denmark, in 1992.

He was with ABB-Scandia, Randers, Denmark, from 1987 to 1988. He became an Assistant Professor in 1992, an Associate Professor in 1996, and a Full Professor of power electronics and drives in 1998. In 2017, he became a Villum Investigator. He has authored or coauthored more than 450 journal papers in the fields of power electronics and its applications. He has coauthored two monographs and edited six books in power electronics and its applications. His current research interests include power electronics and its applications such as in wind turbines, PV systems, reliability, harmonics, and adjustable speed drives.

Dr. Blaabjerg was the Editor-in-Chief of the IEEE TRANSACTIONS ON POWER ELECTRONICS from 2006 to 2012.